INFLUENCE OF BLENDED ELEMENTAL ALUMINUM AND TITANIUM-ALUMINUM MASTER ALLOY ADDITIONS ON THE SINTERING BEHAVIOUR OF TITANIUM – 6 ALUMINUM ALLOY

by

Joannie Lapointe

Submitted in partial fulfilment of the requirements
for the degree of Master of Applied Science

at

Dalhousie University
Halifax, Nova Scotia
October 2016

Dedication Page

J’aimerais remercier mes superviseurs de thèse, Dr. Corbin et Dr. Plucknett, de m’avoir offert une merveilleuse opportunité de me développer dans un domaine qui me passionne, en anglais, et dans une ville qui a beaucoup à offrir.

Finalement, merci beaucoup à ma famille, plus particulièrement à mes parents, Lina et Laval, qui savent me guider, me conseiller et surtout m’inspirer par leurs gestes.

Table of Contents

List of Tables

List of Figures

Abstract

Despite their attractive properties Titanium alloys have limited use in automotive applications due to their high cost. Processing low-cost Ti powder sources through a blended elemental or master alloy powder metallurgy route can reduce cost. This work focuses on the study of the effect of blended elemental and master alloyed Aluminum additions on homogeneity and density during sintering of a Ti6Al alloy. Differential scanning calorimetry, dilatometry, and microscopy are used to study the impact of the Al powder source, size and chemical purity. The combined analysis techniques show that the homogenization is faster with fine blended elemental powder reaching the full homogenized stage after 15 minutes. The densification is better with fine TiAl addition, with an axial shrinkage of over 4%, resulting in an overall densification of more than 12%. These results will help to increase the usage of Titanium alloys and the development of new alloys.

List of Abbreviations Used

APC:	Automotive Partnership Canada
BE:	Blended Elemental
CP-Ti:	Commercially Pure Titanium
DIL:	Dilatometry
DSC:	Differential Scanning Calorimetry
DTA:	Differential Thermal Analysis
EDS:	Energy-Dispersive X-ray Spectroscopy
ΔH:	Enthalpy
HDH:	Hydride-Dehydride
LVDT:	Linear Variable Differential Transformer
MA:	Master Alloy
PA:	Plasma Atomization
PM:	Powder Metallurgical
PREP:	Plasma Rotation Electrode Process
PSD:	Particle-Size Distribution
SEM:	Scanning Electron Microscope
SSS:	Solid-State Sintering
TGA:	Titanium Gas Atomization
VAR:	Vacuum Arc Remelting
XRD:	X-Ray Diffraction

Acknowledgements

The author would like to acknowledge the funding support provided by NSERC through the Automotive Partnership of Canada grant program, with additional funding provided by Wescast Industries Inc and Kingston Process Metallurgy Inc. I would also like to acknowledge the support of the following people: Daniel Cluff, Julian O'Flynn, Clark Murray, Cathy Whitman, Hung-Wei Liu, Nick Koch, Patricia Scallion, Dr. Paul Bishop, and Dr. Darrel Doman.

The author acknowledges the support of the Canada Foundation for Innovation, NSERC, and other partners which fund the Facilities for Materials Characterization, managed by the Institute for Research in Materials.

Chapter 1. Introduction

Fundamental aspects of Titanium, Titanium-Aluminum interactions, sintering in the powder metallurgy process and DSC analysis are discussed in this section.

1.1 Titanium

The element known as Titanium was first identified in 1791, but it was not until 1937 that a process for its extraction and fabrication reached an industrial scale that would allow commercial applications for Titanium. Since then, new Titanium alloys have been developed to fulfill a wide range of applications. Titanium is the fourth most abundant metal in the earth's crust (about 0.6%) after Iron, Aluminum, and Magnesium [1]. Titanium is a transition metal element and is part of the sub-group *IVa* of the periodic table. The elements in this group have four electrons in their outer electronic shell. These elements are chemically reactive and have a tendency to share their outer shell electrons to form covalently bonded compounds [2].

1.1.1 Interest for Titanium

Titanium alloys are very interesting choices due to their particular engineering properties. One of the most important is their high strength-to-weight ratio. This means that their densities are lower than comparable strength alloys. The density of Titanium is only about 60% of the density of steel or nickel-based superalloys. The favorable specific strength ratio of Titanium alloys compared to common engineering alloys is shown in Figure 1.

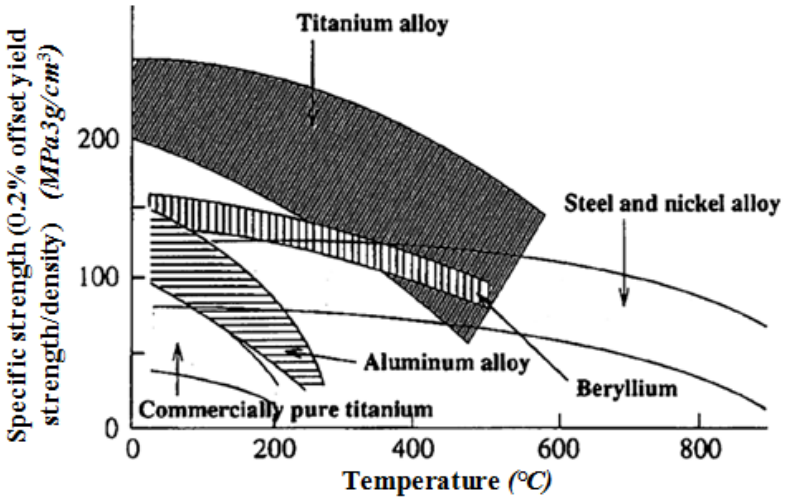

Figure 1 Comparison of specific strength of different alloys [3]

Titanium and its alloys have excellent corrosion resistance; they often exceed the resistance of stainless steel in most environments. Also, their high elevated-temperature properties are attractive for many applications where Aluminum is not sufficient. Finally, Titanium may be processed by means of powder metallurgy technology (P/M), by which route near-net shape products can be achieved [4], [5].

Titanium's major drawback is its high cost, mainly caused by the special manufacturing care required because of its high-reactivity with Oxygen, Hydrogen, Nitrogen and Carbon. However, the cost of Titanium is comparable to that of superalloys [4], [6]. Table 1 compares proprieties of Titanium and its price as a primary material (slug or ingots) to different pure metals and superalloys.

Table 1 Properties comparison [6]–[8]

	Titanium	**Beryllium**	**Aluminum**	**Iron**	**Nickel superalloys**
Density (g/cm^3)	4.54 g/cm^3	1.85 g/cm^3	2.70 g/cm^3	7.87 g/cm^3	8.44 g/cm^3
Modulus of elasticity (GPa)	116 GPa	287 GPa	70 GPa	211 GPa	207 GPa
Melting point (˚C)	1668˚C	1287˚C	660˚C	1536˚C	1350˚C
Price (CAD/kg)	13.95$/kg	1094.85$/kg	1.85$/kg	0.14$/kg	10.74 - 14.11$/kg

Titanium is a light metal and is known for its aerospace applications as jet engine parts or aircraft landing gear beams [6], [9]. Commercially pure Titanium is found in petroleum-processing refineries; an example would be as heat exchanger piping. Highly specialized technical applications, such as sour gas and high-temperature brine or applications that required excellent oxidation resistance and elevated tensile properties, are offered by special Titanium alloys [6].

Titanium is also increasingly found in the automotive industry, mainly because of the weight reduction that is often associated with its use as a replacement for steel. It can be used in the chassis, in the engine, for coils, valves, shafts and most of the fasteners. Titanium's high strength-to-weight ratio permits significant energy economy by the overall reduced weight of the automobile [10].

1.1.2 Effect of Alloying Titanium on Microstructure

Properties of an alloy are affected by the crystal structure, phases, and interstitial elements and are apparent in its microstructure. Chief variables that affect the microstructure of Titanium alloys are processing history, thermal treatment, and very importantly, its chemical composition. Processing history and heat treatments affect most of the mechanical properties (yield strength, hardness, etc.). The type of heating, hold times, type of quenching and mechanical work, are all parameters that must be carefully chosen to achieve the specified mechanical properties.

In agreement with chemical composition, Titanium alloying elements are classified into two categories according to which phase they promote: α-stabilizing or β-stabilizing. β-stabilizing elements tend to be heavier ones, so the density of β-Titanium can be 15% higher than that of α-Titanium [11]. Table 2 presents the main alloying elements (underlined = most important), the main characteristics and the general tendencies of each family of alloys.

Table 2 General properties of different families of Titanium alloys [4], [6]

α-stabilizing elements		**β-stabilizing elements**	
Aluminum, gallium, germanium, oxygen and nitrogen.		Vanadium, iron, molybdenum, tantalum, niobium, silicon, copper, chromium, manganese, nickel and cobalt.	
A	**Near-α**	**α-β**	**B**
Weldable, medium strength, good notch toughness, good creep resistance at elevated temperatures, good corrosion resistance		Heat-treatable, medium to high strength, good forming properties	Heat-treatable, high strength good forming properties, high density

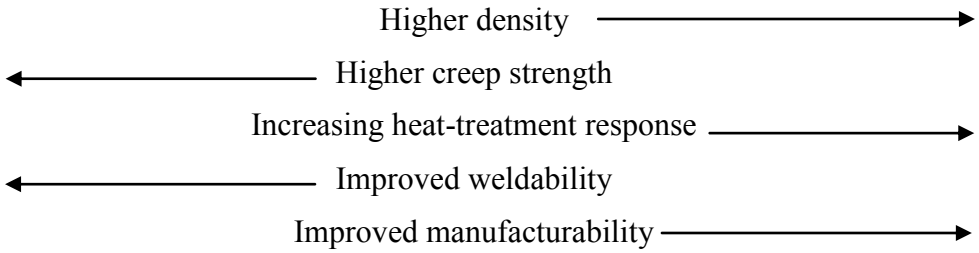

The type of slip systems for dislocation motion in Titanium is affected by the content of interstitial elements, like Oxygen or Nitrogen, with concentration as low as 0.1wt% of interstitial elements. At this concentration, slip occurs mainly on the $\{10\bar{1}1\}$ pyramidal plane. Oxygen content is a reliable indicator of strength in CP-Ti, but Oxygen also reduces the fracture toughness of Titanium. An increase of impurities levels causes Titanium to be more brittle with because of interstitial strengthening. Figure 2 shows that elemental impurities decreased Titanium's ability to withstand a reduction in area. When high-toughness is required, extra-low interstitial CP-Ti is used.

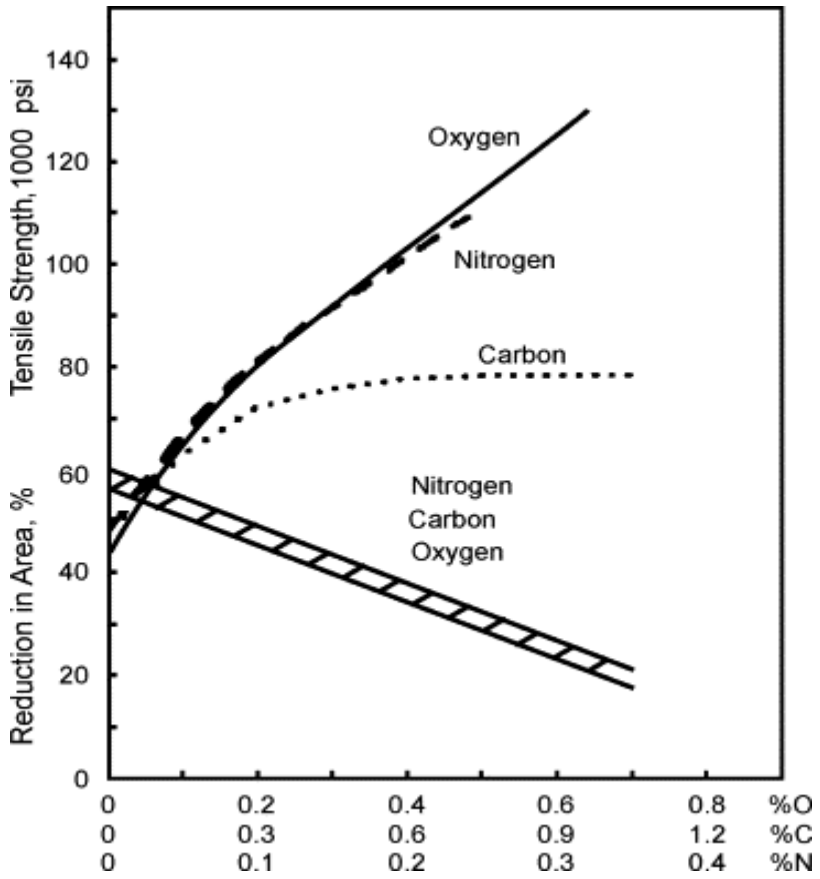

Figure 2 Effect of Titanium interstitial alloying elements on strength and reduction in area [12]

1.1.3 Titanium Phases

Titanium has two different stable phases in the solid state, α-phase a hexagonal close-packed (HCP) crystallographic structure and β-phase a body-centred cubic (BCC) crystallographic structure, and one metastable phase, ω-phase a hexagonal (distorted bcc) structure. At room temperature, Ti undergoes a phase transition from the stable α-phase to the metastable ω-phase at about 77 kbar, as shown in Figure 3 by two different studies [2], [13]. However, in conventional industries, the pressure is usually held constant at a low value as the temperature is raised. Therefore, the α to β phase transition is the most important in conventional process engineering.

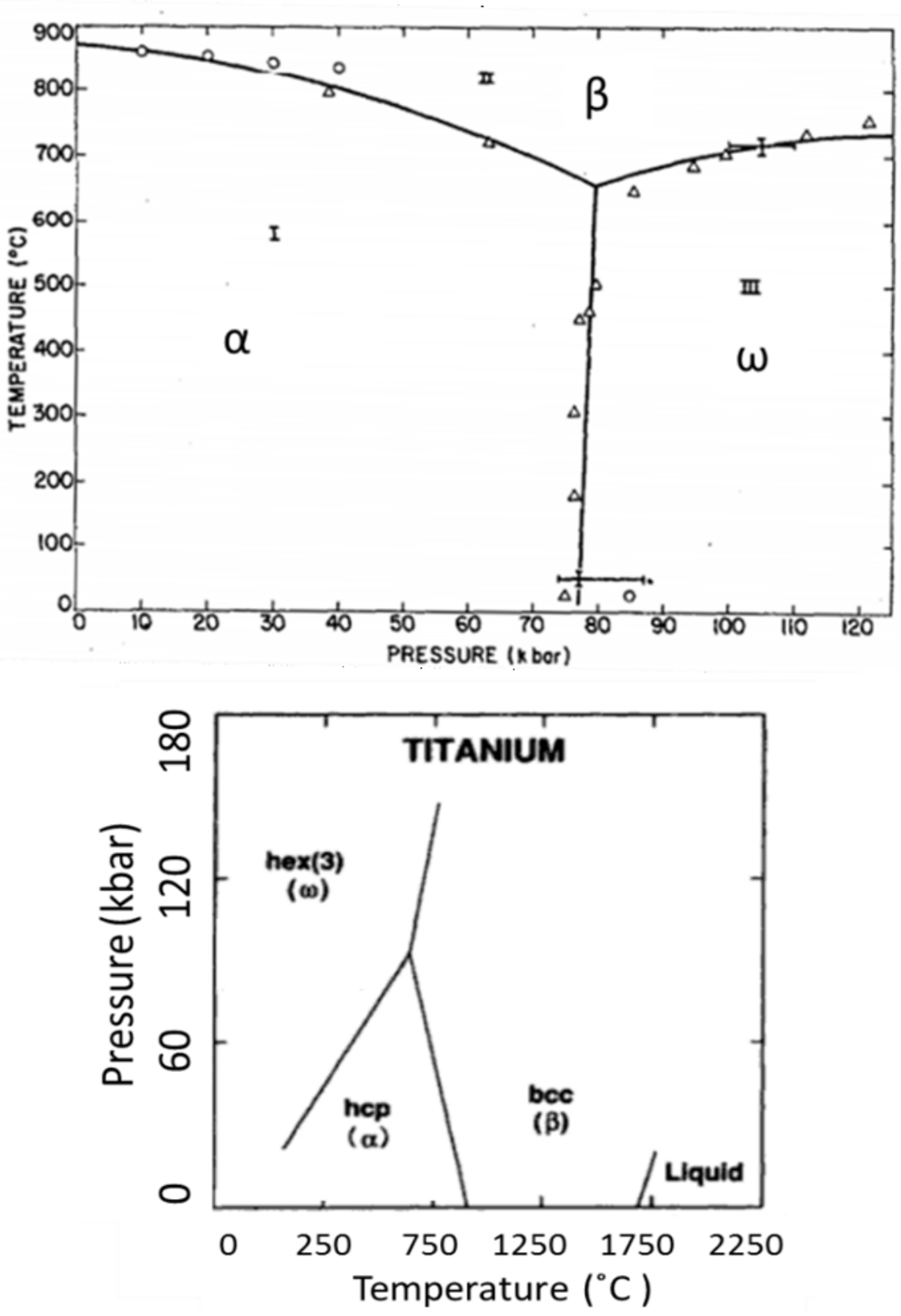

Figure 3 Phase diagrams for Titanium [2], [13]

Figure 4 presents the effect of different alloying elements on the temperature of the phase transition in Titanium alloys. These different effects can be additive in multi-element alloys, as it is shown in Figure 5. Each diagram represents a family of Titanium alloys from Table 2, and the family name is relevant to the phase promoted by the addition of alloying elements.

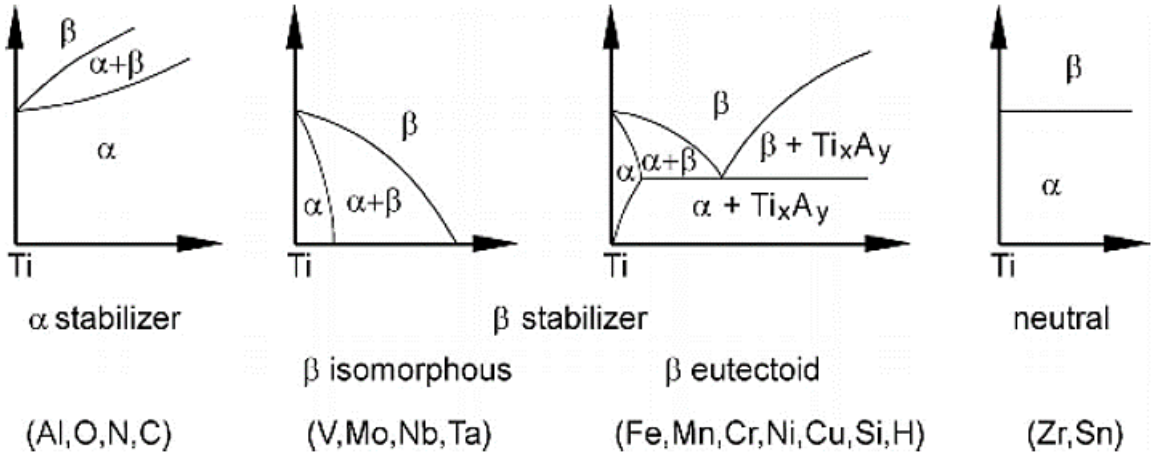

Figure 4 Effect of alloying elements on phase diagrams of Titanium alloys (schematically) [1]

Some technical Titanium alloys are presented in Figure 5 and are sorted according to their family. Most of them are α-β alloys with a concentration between 6 to 8% of Aluminum with different added elements. In the metastable β alloy area, the Aluminum concentration is 3% or less.

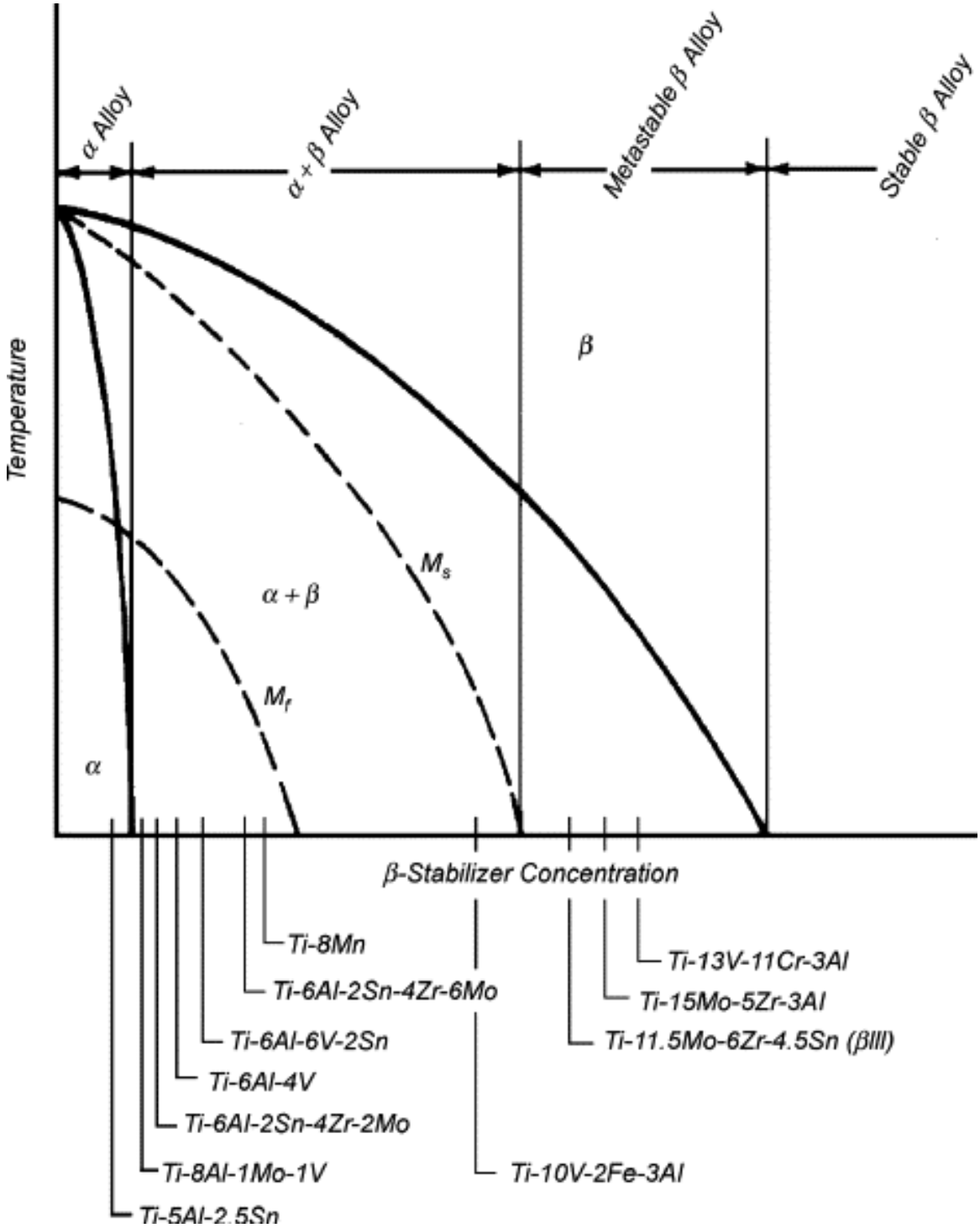

Figure 5 Compositions of U.S. technical alloys mapped onto a pseudo binary β-isomorphous phase diagram [14]

1.1.4 Titanium Production and Refining

Ores containing Titanium include rutile (97% of TiO_2) and ilmenite ($FeTiO_3$) [4], [15]. Iron is extracted from ilmenite, and the slag left contains a high-density of Titanium dioxide, which can be further chemically processed.

All Titanium refining processes have the same starting point: Titanium dioxide is chlorinated to form $TiCl_4$. Then, the most common technique is the Kroll process. It uses magnesium to reduce the $TiCl_4$. The quantity of magnesium needed to reduce all the $TiCl_4$ is used, plus a buffer. Magnesium is heated up to 800-900˚C and then the $TiCl_4$ is slowly incorporated [6]. The following reaction happens:

$$TiCl_4\ (gas) + 2Mg\ (liquid) \rightarrow Ti\ (solid) + 2MgCl_2\ (liquid) \qquad \text{(I)}$$

When all the $TiCl_4$ is reduced, the pressure rises. The Titanium metal formed is a porous mass that resembles a sponge that will be further mechanically processed [16].

Another typical process is the Hunter process. It uses sodium instead of magnesium. It has the advantage that it can be carried out in two steps as shown in equation II. The Hunter process is more expensive than the Kroll process, and it is generally used when a higher level of purity is required [6], [16].

$$\begin{gathered} TiCl_4 + 2Na \rightarrow TiCl_2 + 2NaCl \\ TiCl_2 + 2Na \rightarrow Ti + 2NaCl \end{gathered} \qquad \text{(II)}$$

There are many new technologies that have been developed or investigated, in the last decades, to reduce the costs of Titanium production and deliver products closer to their final form. The two most known and discussed are the FFC Cambridge process and the Armstrong process [15], [16].

The FFC Cambridge process relies on electrolytic reduction. It uses pure rutile (TiO_2) pressed into pellets as a cathode in a 950˚C calcium chloride ($CaCl_2$) bath. A current is applied between the cathode and a graphite electrode, used as the anode. Under that current, the Oxygen is ionized and dissolves into the $CaCl_2$ bath, as shown in Figure 6.

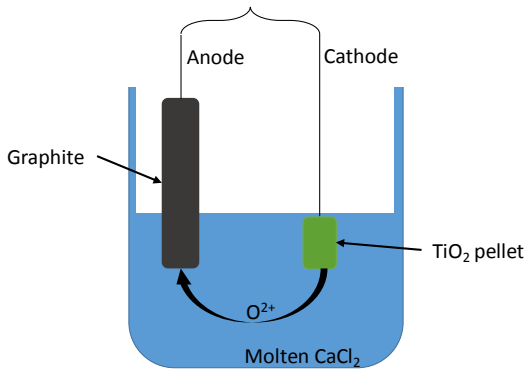

Figure 6 FFC Cambridge process illustration [15], [17]

The Armstrong process is an in-line deviation of the Hunter process. Titanium tetrachloride ($TiCl_4$) vapour is injected, to form powder directly, into a stream of molten sodium in sufficient quantity to reduce all the Titanium. Filtration, distillation, and washing remove the excess of sodium and salt (NaCl) [15]. Since it produces high purity useable powder (it can even produce alloyed powder), the use of this process has expanded a lot since the beginning of 21st century.

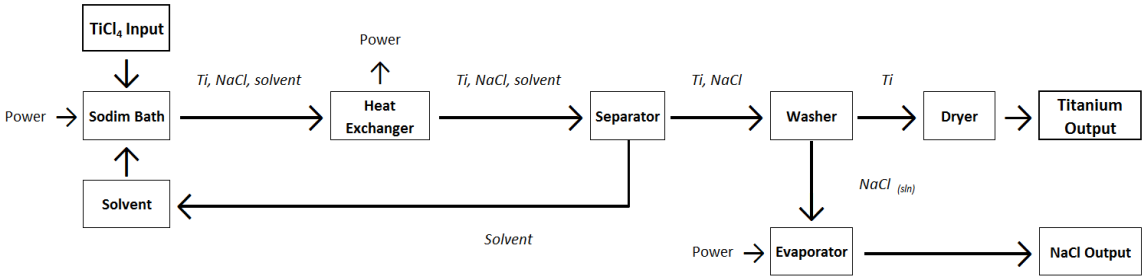

Figure 7 Diagram representing Armstrong overall process [15]

Titanium sponge formed, except by Armstrong process which directly forms the powder, is crushed into small particles and compacted into a mold. The compacts are then welded together to form a long consumable electrode to achieve vacuum arc remelting (VAR). The use of a vacuum is crucial because Titanium's reactivity with an atmosphere would produce undesirable components. If Titanium alloys are needed, alloying particles are added to the mixture prior to welding. It can be necessary to melt and solidify the alloy more than once to ensure the homogeneity of the final product [6].

1.1.5 Titanium Powder Production

Net shape is an interesting cost reduction opportunity offered by powder metallurgy (PM) because this manufacturing process uses less material (buy-to-fly ratio) and it necessitates less machining [18]. There are many technologies to make Titanium powder from the primary metal. The Hydride-Dehydride (HDH) process is the most commonly used. Figure 8 shows the different steps followed by the Titanium.

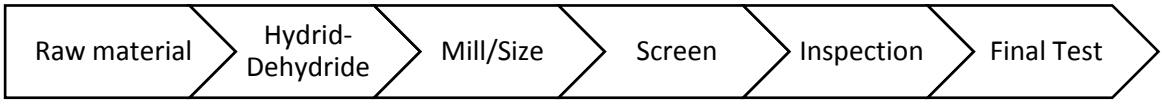

Figure 8 Hydride-Dehydride Process [19]

The raw material can either be purified sponge fines or the further processed VAR product. As written in equation III, a Titanium dihydride is formed. The hydride is very brittle so it can be easily milled to a fine powder. It is then screened to the specified particle-size distribution (PSD) [19].

$$Ti\ (solid) + H_2\ (gas) \rightleftharpoons TiH_2\ (solid) \qquad \text{(III)}$$

The other powder production techniques are the plasma rotation electrode process (PREP), Titanium gas atomization (TGA) process and plasma atomization (PA) process [20]. The cost of these processes is higher than HDH process, which is more commonly and widely used.

A bar of pure or alloyed Titanium is rotated and slowly melted for PREP. This process produces high-quality Titanium powder for specific applications. The rotation causes the centrifugal atomization of droplets that solidify in an inert gas.

In the TGA process, molten metal is poured as a tiny stream into high-pressure jets of inert gas. The gas flow fragments the stream into fine particles that are instantly solidified to atomized powder.

Finally, in the plasma atomization process, plasma torches are used to melt a wire of Titanium metal and the molten metal is then atomized in an inert atmosphere. Table 3 presents the specifications of those techniques.

Table 3 Main powder production techniques [4], [19], [20]

Techniques	Powder size	Applications
HDH	50-300 µm (angular)	Non-critical applications
PREP	100-300 µm (spherical)	Aeronautic, biomedical
TGA	50-350 µm (spherical)	Metal injection molding, filters, etc.
PA	5-250 µm (spherical)	Biomedical

1.2 Titanium-Aluminum Binary Phase Diagram

As presented in section 1.1.2, Aluminum is the most important α-stabilizing element for Titanium alloys [4], [6] being used in 9 of the 11 alloys listed in Figure 5. Aluminum is light (2.70 g/cm3), thus decreasing the overall density, and improves the strength of the alloy by adding solid-solution strengthening. The Titanium-Aluminum phase diagram is presented in Figure 9.

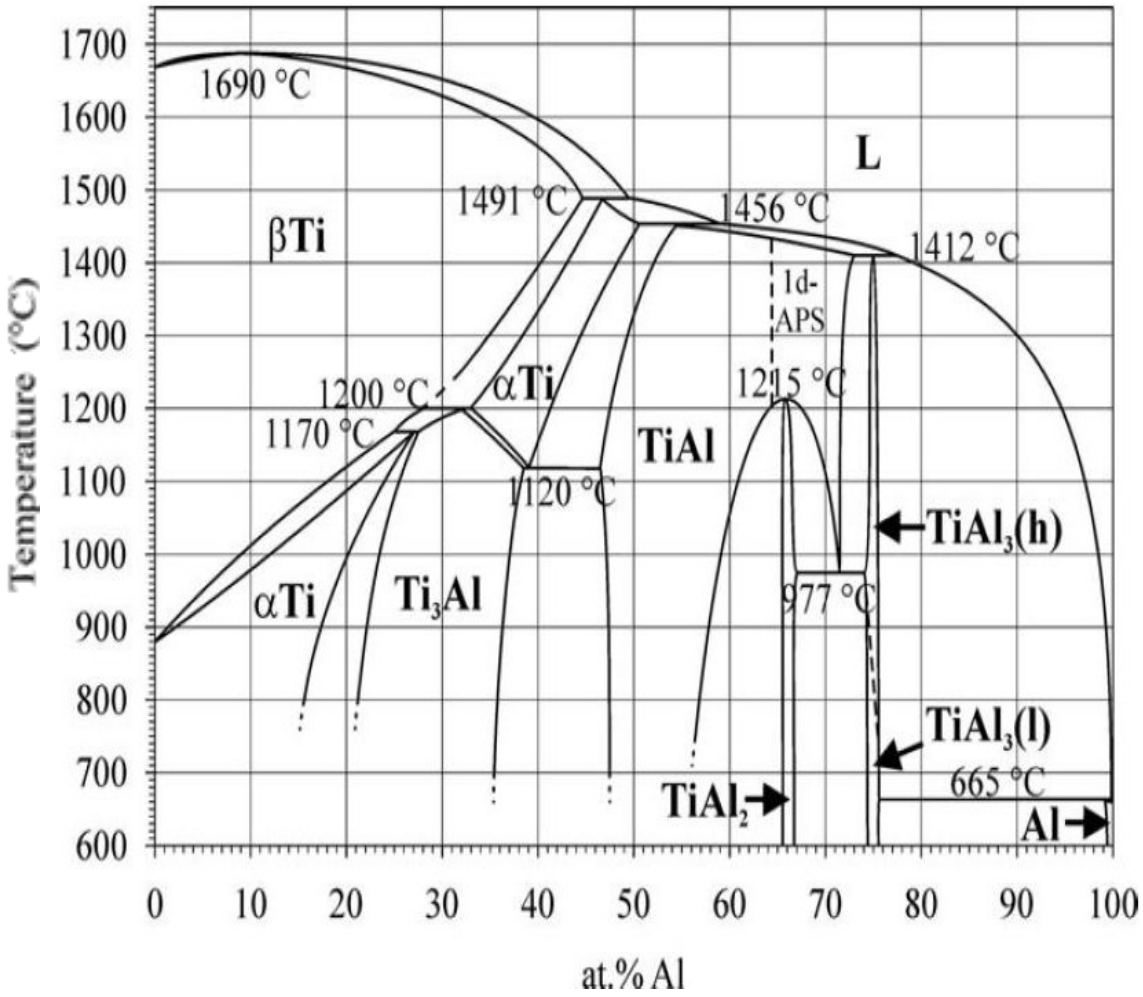

Figure 9 Titanium-Aluminum phase diagram [21]

The melting point of Titanium is 1668˚C while the melting point of Aluminum is 660˚C. Adding a small amount of Aluminum raises the α-Ti to β-Ti transformation temperature, from 882°C [22], up to 1170˚C depending on the amount added. There is a plateau, at high concentration of Al, at 665˚C between solid and liquid Al + $\alpha TiAl_3$.

1.2.1 Titanium and Aluminum Intermetallics

The major intermetallics formed between Al and Ti are Ti_3Al, TiAl, $TiAl_2$ and $TiAl_3$. It is generally accepted that $TiAl_3$ is a line compound [23], [24], but Kattner *et al.* [25] considered $TiAl_3$ to exist over a range of composition. New alloys from Titanium aluminide (TiAl) are currently developed for their high operational temperature, but they have a lower ductility and formability than low Aluminum Titanium alloys [4].

Figure 10 presents the free energies of formation of the five Titanium-Aluminum intermetallics. Formation of $TiAl_2$ and Ti_2Al_5 requires the previous formation of $TiAl_3$ [24]. TiAl has a steep slope on the temperature range. Higher temperatures result in less favorable conditions for the formation of TiAl.

The Aluminum content in Titanium alloys usually remains below 6wt% to avoid a rapid decrease in the alloy's ductility due to too much Ti_3Al intermetallic formation, as can be seen on Figure 9.

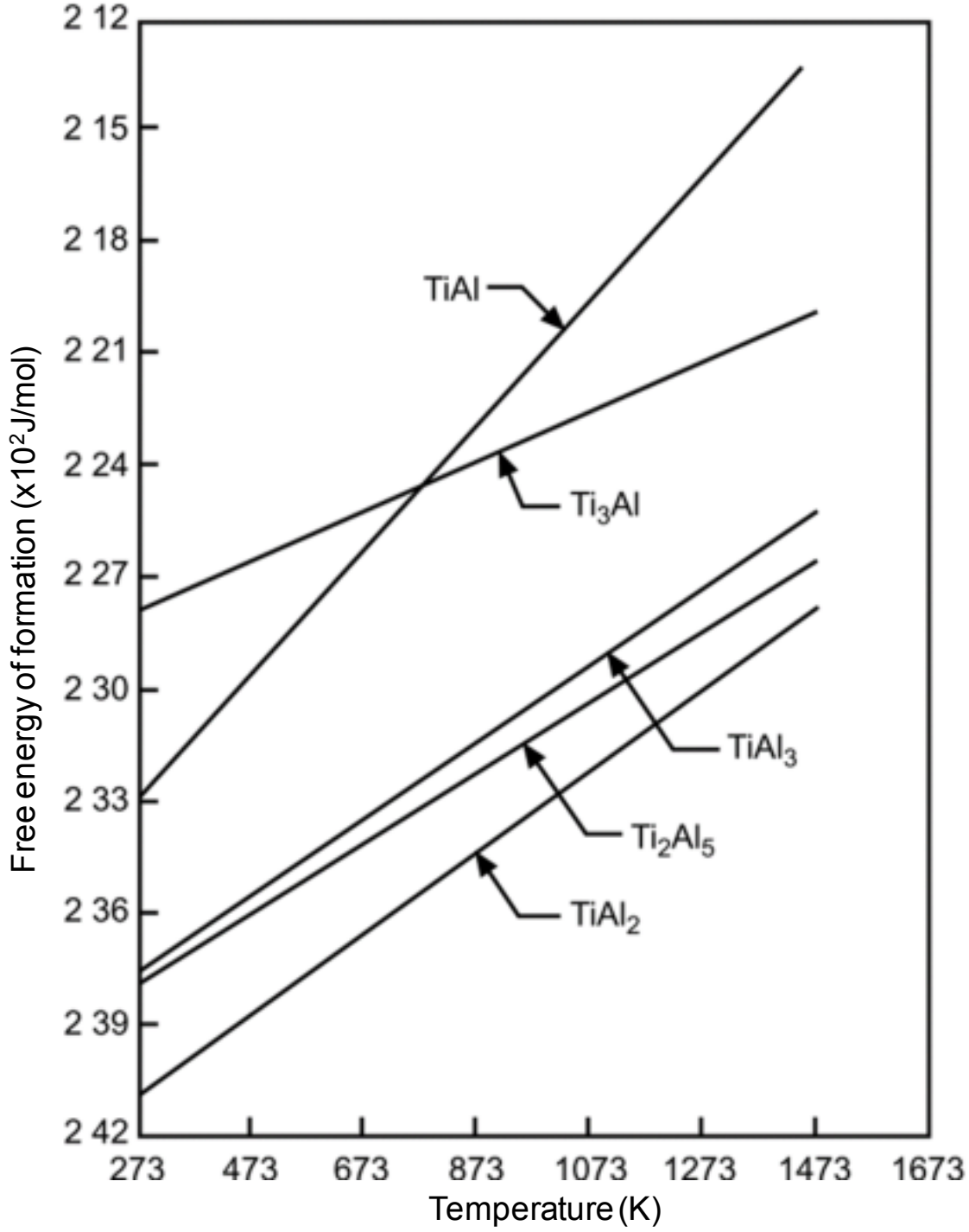

Figure 10 Free energies of formation of different Ti-Al intermetallics as a function of temperature [24], [25]

1.3 Elemental Impurities

Titanium has a high chemical affinity to Oxygen, which causes the rapid oxidation of Titanium. Oxidized Titanium is brittle, has low ductility and low fatigue resistance [1]. Figure 11 presents the Oxygen-Titanium binary phase diagram. A very low percentage of Oxygen in the Titanium alloy increases the α-to-β transformation temperature sharply.

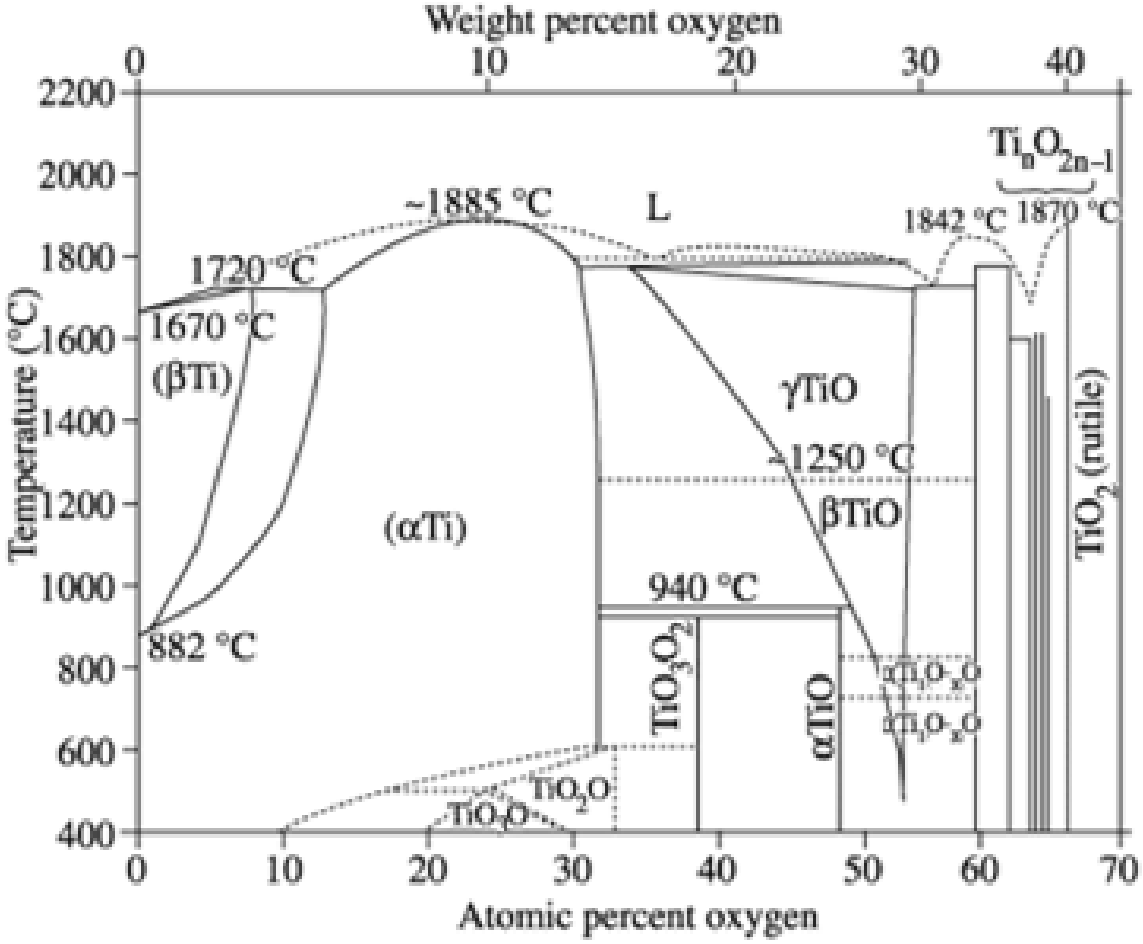

Figure 11 Oxygen-Titanium binary phase diagram [26]

Figure 12 presents the Nitrogen-Titanium binary phase diagram. Similarly to Oxygen, Nitrogen increases the α-to-β phase transformation temperature of Titanium alloys. However, the driving force of Titanium to Nitrogen is lower than for Titanium and Oxygen [1].

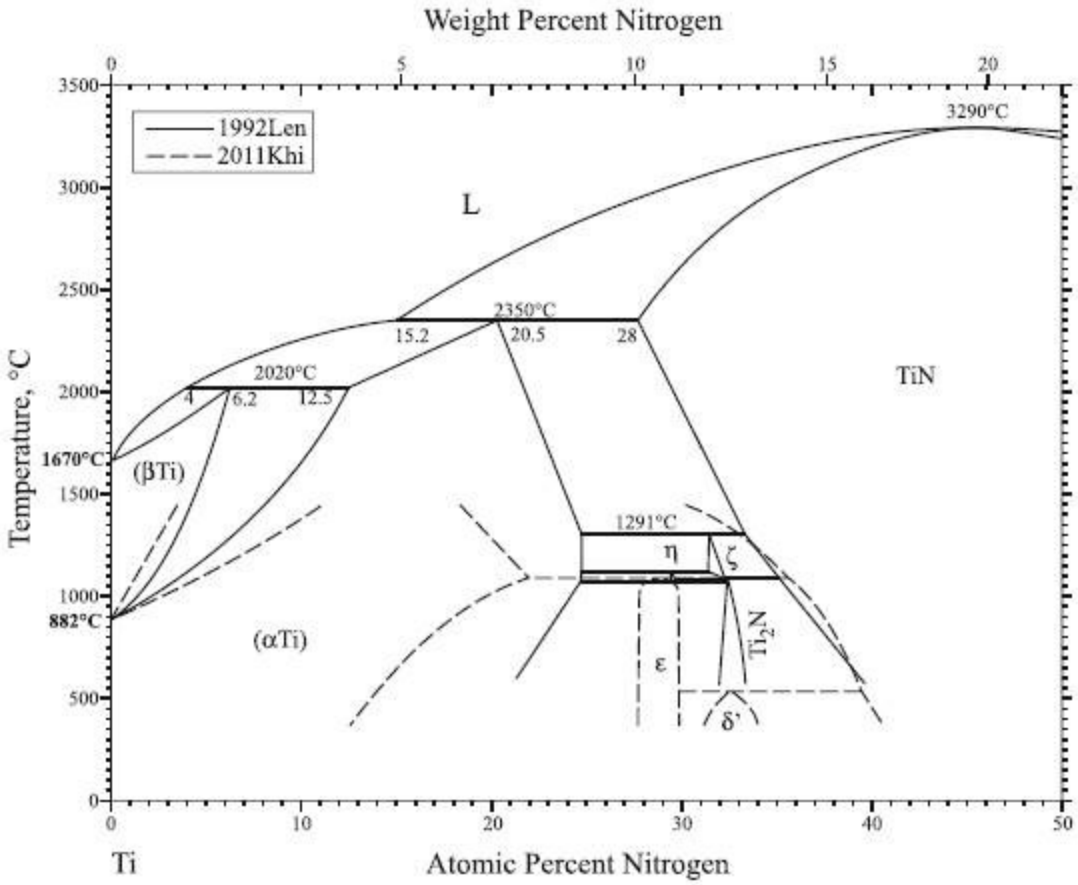

Figure 12 Nitrogen-Titanium phase diagram [27]

1.4 Sintering

In the sintering process, the metal powder is heated to produce a dense part. There are two major sintering processes: liquid phase sintering and solid-state sintering, as shown in Figure 13. Powders are blended to form the desired alloy and then heated below the liquidus temperature of that alloy for a certain time for those powders to fuse.

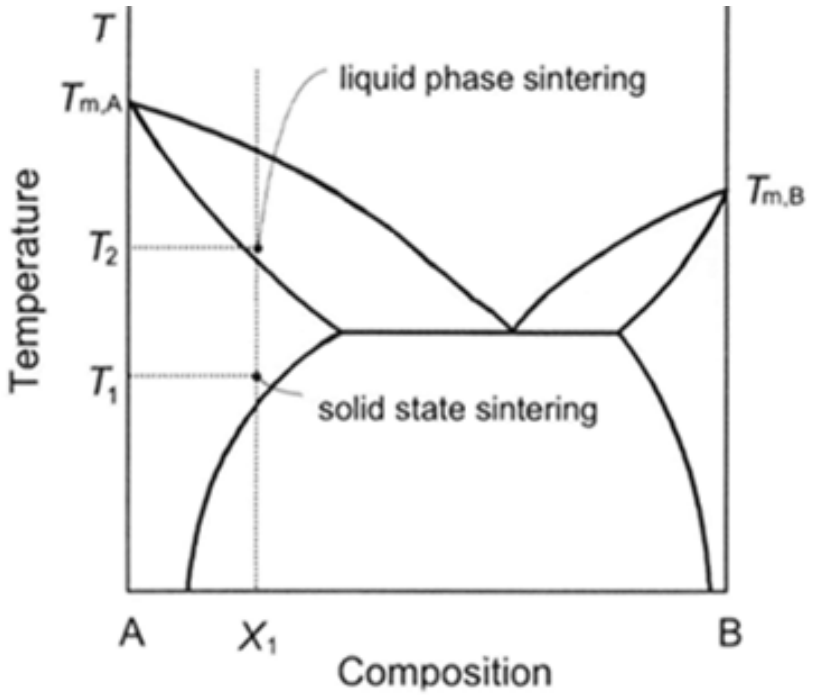

Figure 13 Illustration of various type of sintering [28]

The surface area, the neck size ratio, the final density, and shrinkage are related measures of the pore elimination process during sintering. Those measures help to predict the final properties. Sintered part properties can range from a very dense part with high mechanical properties for a transmission gear, to a very porous cohesive part for a gas filter.

There are three possible powder inputs: pure elemental powder, master alloy powder and fully-alloyed powder. The fully-alloyed powder is relatively expensive and will not be studied in the scope of this work. Table 4 presents the characteristics of the powder sources of interest.

Table 4 Characteristics of the alloying additions in powder metallurgical processing [29]

Powder type	**Elemental**	**Master**
Cost	Economical	Expensive
Composition adjustment	Very easy	Difficult
Hardness	Soft	Harder
Chemical gradient	More	Less

In addition to these powder types, specific attributes like size, shape, and packing must be determined to achieve high performance shaped products [30]. The process under investigation in this research work is under the classification of solid-state sintering, which is the focus of further discussion below.

1.4.1 Solid State Sintering

As shown in Figure 13, solid-state sintering (SSS) occurs at an elevated temperature but under the solidus temperature formation. SSS affects the material properties (i.e. loss of mechanical properties caused by grain growth) less than liquid phase sintering [28].

There are three stages overlapping in SSS as shown in Figure 14: initial, intermediate and final. They can be identified under an optical microscope by looking at physical characteristics like neck formation and pore distribution [28].

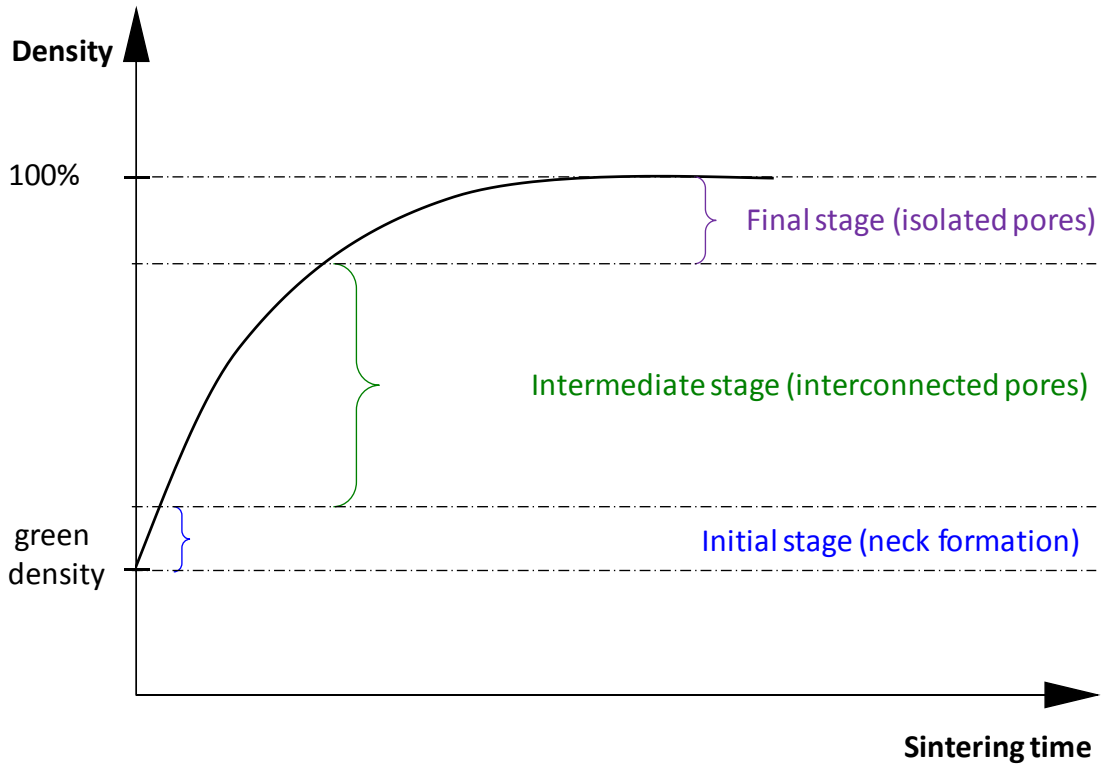

Figure 14 Sintering stages and densification curve of a powder compact [28]

1.4.1.1 Initial Stage Sintering

As shown in Figure 14, the initial stage has only a small impact on the global increase in density because of the nature of the phenomena involved. Material transport, which causes the formation of necks, is affected by two different mechanisms: surface transport with no effect on the density and bulk transport which helps densification by shrinkage. Those mechanisms are, primarily, diffusion processes that depend on atom motion, which itself depends on the thermal energy of activation. When an atom gains enough energy to break free from its current site, it is able to move into a vacant site. Sintering is faster at higher temperatures, because of the increased number of active atoms and available sites.

The particle size, temperature and time are all characteristics that affect material transport mechanisms. Small particles sinter faster than large ones because they have more surface energy which enhances surface and grain boundary diffusion. Temperature is a trigger for sintering and once the reaction has started it has a large effect on the sintering rate.

Figure 15 presents the two-spherical particles model for various transport phenomena. Each phenomenon involves volume diffusion but differs with the other diffusion processes.

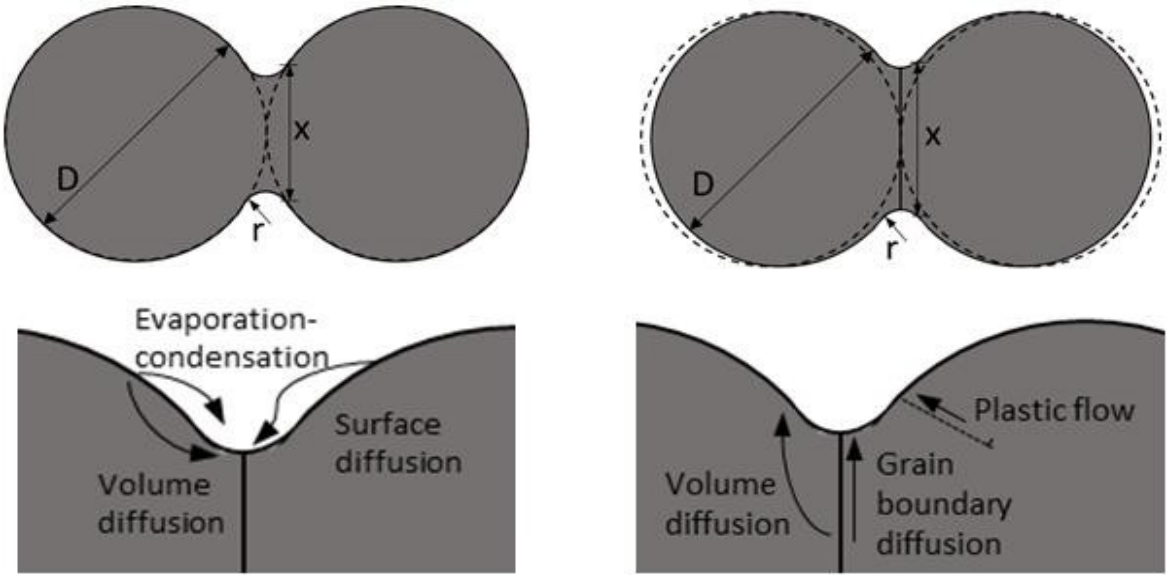

Figure 15 Two-sphere sintering model – Left: surface transport (without shrinkage), Right: bulk transport (with shrinkage) [28], [30]

Surface curvature of particles creates differences in bulk pressure, vacancy concentration, and vapour pressure. Those differences are the driving force of SSS. Surface diffusion eliminates the high surface energy associated with a fine powder. At each contact of particles a grain boundary, a lower energy interface, grows by diffusion to replace the solid-vapour interface.

The concave curvature of the neck region allows the vapour pressure over it to be lower than the equilibrium condition. The particle is convex, so the vapour pressure over it is higher than the equilibrium condition. Evaporation-condensation then causes a net mass flow into the neck region.

1.4.1.2 Intermediate Stage Sintering

As shown in Figure 14, the intermediate stage is most important for the part densification during SSS. It is characterized by pore rounding and grain growth. To visualize the pore shrinkage, a model illustrating pores as channels has been developed and is presented in Figure 16. It assumes equal shrinkage of pores in the radial direction and does not take the grain growth into consideration.

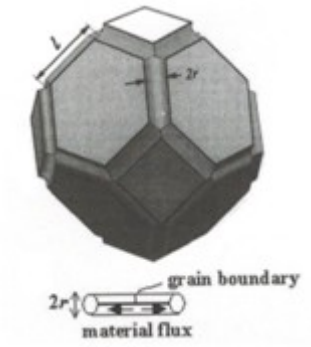

Figure 16 Channel pore model [28]

Volume and grain boundary diffusion, started in the initial stage, help with densification in the intermediate stage. Pores located on grain boundaries disappear more rapidly than isolated pores. Pore rounding and pore migration along the grain boundaries is caused by surface transport. As stated in the previous section, the surface transport processes do not contribute to densification or shrinkage.

Temperature influences the rate of diffusion, grain growth, and pore motion. In many materials, those rates are also dependent on the specific morphology (grain size, pore size, and pore spacing). As the microstructure is continually changing, the temperature has a complex influence on the sintering process.

1.4.1.3 Final Stage Sintering

Most of the densification occurred during the intermediate stage, so the final stage only has a small influence on the overall densification, as shown in Figure 14. In the final stage, the spherical pores shrink by a bulk diffusion mechanism. The isolated pore model, shown in Figure 17, is used to illustrate the pore isolation on grain corners.

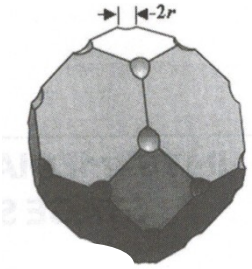

Figure 17 Isolated pore model [28]

Grain boundary breakaway occurred in the intermediate stage leaving behind spherical pores. This slows the shrinkage process because pores must rely on bulk diffusion which is controlled by vacancy concentrations now that the pores are not linked by channel grain boundaries. Long sintering time coupled with specific conditions can lead to an undesired decrease in densification.

1.5 Differential Scanning Calorimetry

1.5.1 DSC Technology

Differential scanning calorimetry (DSC) measures characteristic temperatures and heat flow rates (power) associated with transitions in materials as a function of time and temperature [31], [32]. There are two types of DSC shown in Figure 18: power-compensated DSC and heat-flux DSC.

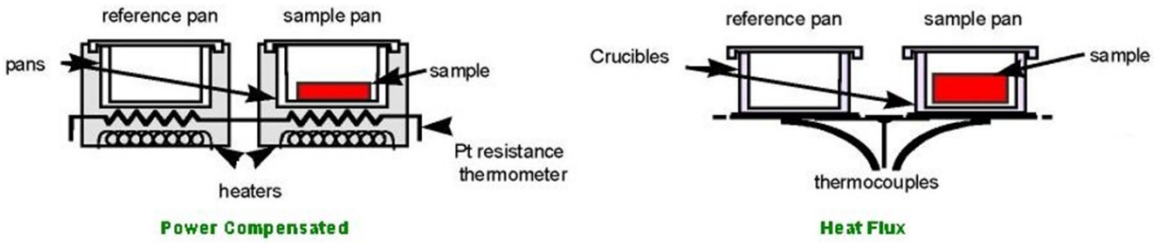

Figure 18 Schematic drawing of DSCs [31]

Power compensated DSC measures the power difference between the reference and the sample. The sample and the reference are placed in two identical furnaces, following the same temperature program, but the transitions in the material create heat difference between them that is compensated by electrical power in the sample furnace, which is recorded. Heat-flux DSC is part of the differential thermal analysis (DTA) family. DTA is used to measure the temperature difference between the sample and the reference, which are placed in the same furnace, as a function of temperature (or time) [32].

1.5.2 Theory of Heat-Flux DSC

DSC measures the difference between the heat flow from the sample crucible and the heat flow from a reference crucible. These two crucibles, shown on a crucible carrier in Figure 19 for a heat-flux DSC, are exposed to the same thermal conditions as they are in the same furnace.

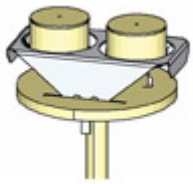

Figure 19 Reference and sample crucible carrier for heat-flux DSC [33]

For a heat-flux DSC, the thermocouples are measuring the difference in temperature (ΔT) between the two crucibles. The measurement signal ΔT is obtained as an electric voltage. To obtain the heat flow rate, Φ_m, ΔT has to be adjusted by a calibration factor, k', as shown in equation (IV).

$$\Phi_m = -k' * \Delta T \quad \text{(IV)}$$

The final measurement signal output by the DSC, accessible to the user, is this calculated Φ_m (mW) [32]. The k' constant is obtained experimentally by measuring the melting temperature and enthalpy of high purity standards. The calibration factor is then calculated by correlating the measured values with the known enthalpy and melting point of those standards. Standards are chosen such that their melting point falls in the temperature range of the equipment.

The two crucibles are on the same carrier in the same furnace and disturbances such as temperature variations in the environment affect them in the same way. In every type of DSC, heat flow rate is due to a change of the sample temperature compared with the reference crucible temperature: when the ΔT is zero there is no net heat flow rate.

Any reaction in the sample is due to a change in enthalpy (ΔH), either negative or positive. An endothermic reaction involves a positive change in enthalpy, $\Delta H > 0$, and a negative change in enthalpy, $\Delta H < 0$, is an exothermic reaction. For an endothermic reaction, the net heat flow is from the environment to the sample, as the sample absorbs energy, and for an exothermic reaction, the net heat flow is from the sample to the environment. The thermodynamic events that are recorded by a DSC include melting, phase transition, thermal decomposition and glass transition.

1.6 Dilatometry

Dilatometry (DIL) is the study of the change in length of a specimen during heating. The technique can be referred to as thermo-mechanical analysis, and records the change in length as a function of time or temperature [34].

Specific events during the heating or cooling process of a sample can be detected with the dilatometer, like phase transformations, since specific volumes of the untransformed and fully transformed phases are often different. Also, each phase has its own coefficient of thermal expansion which can lead to additional length change in the compact [34].

Figure 20 presents the main components of a dilatometer. The furnace chamber is sealed, with two valves, and can be kept under tight vacuum by shutting off the outlet valve or under a constant gas flow by forcing a constant volume of inert gas into the chamber with

the outlet valve open. Within the chamber, the sample is placed in a cradle-like support made from alumina and by two alumina protective spacers at both ends of the sample. The heating element is surrounding the sample, heating the chamber uniformly. The dilatation of the sample moves the push rod, which transmits the movement to the linear variable differential transformer (LVDT) to relay the information to the computer.

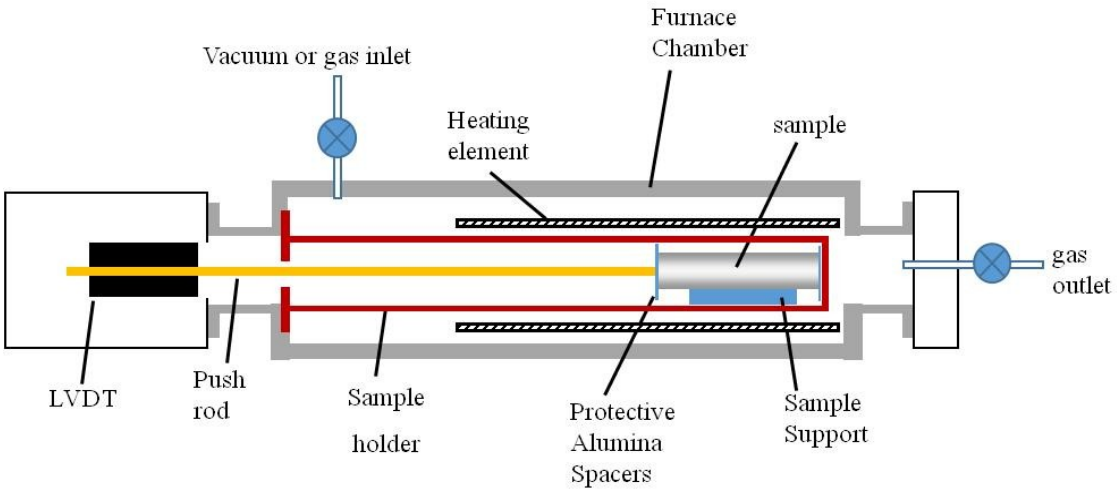

Figure 20 Schematic of the dilatometer

Dilatometry (DIL) and calorimetry (i.e. DSC) are both useful to record phase transformations. Some phase transformations can generate a large change in specimen length, in which case DIL would be the most sensitive, while DSC would be more sensitive for other phase transformations with a large exothermic/endothermic reaction [34].

Chapter 2. Research Objectives and Titanium – Aluminum Powder Metallurgical Studies

Automotive Partnership Canada (APC) is a grouping of university researchers and automotive companies that are collaborating through R&D activities for the benefit of the entire Canadian automotive industry. In order to decrease the automotive energy consumption and to increase the manufactured parts service life, one of the APC research aims is to make Titanium an affordable alternative to replacing steel in cars [35]. Titanium is lighter than steel for the same strength and is resistant to corrosion.

To achieve this project, it is necessary to demonstrate how to make cost effective and efficient finished pieces out of Titanium alloys. One consideration is to take Titanium powder from the raw form and sinter it into a finished part. In a recent review McCracken [36] points out that there are many fabrication routes to produce Ti powder. The most cost effective and commercially available is the HDH process. Within this method, particle sizes in the range of 45 to 150 μm offer the best combination of cost and purity levels. However, this relatively coarse particle size can offer challenges in terms of sinterability [37]. Therefore a study of the sintering behaviour of these powders is very important.

CP-Ti HDH powders are the most readily available commercially and offer an effective feedstock for producing a range of PM alloys through either blended elemental (BE) or mater alloy (MA) sintering. MA and BE sintering must demonstrate adequate chemical homogeneity and sintered compact density to be considered a suitable manufacturing process. Chemical homogeneity and density evolve through the sintering time. Determining the optimal heating time and temperature for each powder source will lead to an optimized thermal process.

The sintering behaviour of powder metallurgical Titanium alloys was studied by several groups, focusing mainly on Ti64 [38]–[41]. Most articles treated issues surrounding full density and homogenization with regard to either impurities, particle size, nature of alloying addition and sintering temperature [37]. Other studies focused on microstructural evolution during sintering of Titanium alloys [42].

Products made from complex or new alloys are sintered from BE or MA alloy additions for economical reasons or because prealloyed powders are not available [20]. As Figure 5 points out, 9 out of 11 of the most common Ti alloys used commercially contain Al in the range of 3 to 8wt%. The many combinations of elements in the listed alloys would make it very challenging to identify Al containing MA additions with the correct composition. Therefore, ways in which to add only Al to a CP-Ti mixture either through BE or Ti-Al MA methods are needed in order to advance the low cost PM route for Titanium alloy production.

Chemical homogeneity and compact density of blends with a single Aluminum addition needs to be first analysed and understood. This step will help understand the behaviour of more complex BE or MA mixtures made to produce alloys such as Ti6242, or the development of new commercial alloys like Ti-5Al-2.5Fe. A thermodynamic binary elemental study has been conducted on Ti-2.5Fe [43] but not on the Titanium-Aluminum binary system.

At the moment, only one study of the a Titanium-Aluminum binary BE alloy addition is reported in the literature [44]. In this study, the concentration of Aluminum changed from 2 to 5 wt%, but the powder size was kept constant at -325 mesh. They found that the formation of intermetallics, which were formed by the melting of Al, had a strong influence on the sintering, which ends with Ti grain boundary diffusion.

Thermodynamic study of the α-to-β phase transformation was conducted by a pulse heating method, first in pure Titanium rods [45]. Since then, more DTA work was done on powder metallurgical compacts, often ternary systems like Ti64 [38], [39] or Ti-43Al-5V-4Nb (at%) [46].

The precise objectives of this work are to study the effect of the powder size and form, BE or MA, on the homogenization and densification of Titanium-6Aluminum. DSC thermograph analysis will be used as the primary tool for the study and the results will be confirmed by optical microscopy, scanning electron microscopy and dilatometry. DSC thermograph analysis has been used only in a limited amount of studies in the powder metallurgical field.

Chapter 3. Materials and Methodology

3.1 Powders

Commercially pure Titanium (CP-Ti) was used as the matrix. It was manufactured by Reading Alloys by a hydride-dehydride (HDH) process and conforms to ASTM Grade 3. It was chosen as a compromise between purity and cost, optimal for the automotive industry.

Coarse and fine elemental Aluminum powders were procured from ECKA Granules. A master alloy TiAl (50:50 atomic percent) powder was procured from Alfa Aesar. The master alloy powder was manually sieved for 15 minutes according to the procedure outlined in section 7.3 of ASTM B214-07 (2011) [47]. The sieves were 3.25 inches in diameter and 1 inch deep to accommodate the small amount of powder used. Canadian standard sieve series 200, 325, 400, 450 and 500 mesh sieves were used.

The powders are presented in Table 5. The particle size distributions (PSD) of the additions are presented in Appendix A. Carbon (C), Hydrogen (H), Oxygen (O) and Nitrogen (N) impurity levels for all powders under investigation were analyzed by an independent laboratory.

Table 5 Definition of the powders used

Role	Composition	Supplier	Size	Chemistry [3,4] (wt%)			
				C	H	O	N
Matrix	Titanium (CP-Ti)	Reading Alloy	D_{50} = 109.9 μm[1]	0.010	0.012	0.179	0.010
Master Alloy	TiAl-coarse	Alfa Aesar	> 45 μm[2]	0.155	0.033	0.50	1.060
Master Alloy	TiAl-fine	Alfa Aesar	< 25 μm[2]	0.096	0.017	0.94	0.350
Elemental	Al-coarse	ECKA	D_{50} = 43.1 μm[1]	0.006	0.006	0.132	0.002
Elemental	Al-fine	ECKA	D_{50} = 12.7 μm[1]	0.011	0.015	0.54	0.003

[1]Analysis by Dalhousie Mineral Engineering Center
[2]Manually sieved
[3]Analysis by Wah Chang Labs
[4]Refer to Appendix B for TiAl-coarse

CP-Ti was mixed with either MA TiAl or BE Aluminum to a concentration of 6wt% Al. The powder mixtures were dry milled for 60 minutes in a glass jar. Hereafter the powder mixtures will be referred to according to the nomenclature presented in Figure 21.

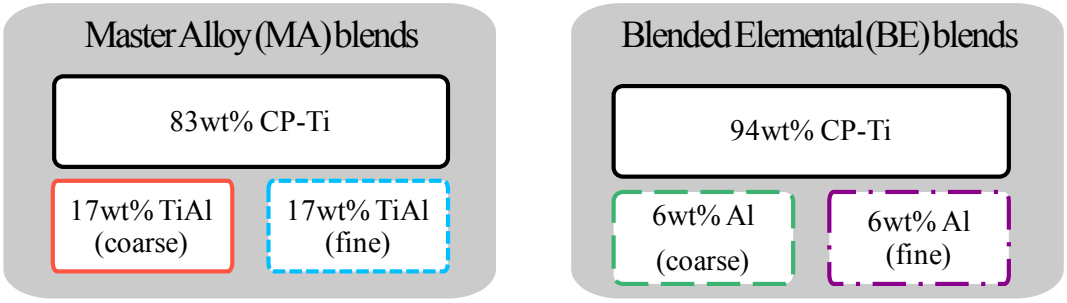

Figure 21 Powder blends studied (weight percentage)

The chemistry reported in Table 6 was calculated based on the mass fraction of the individual powders. Details are given in Appendix C.

Table 6 Nomenclature of the powder blends and their chemical impurities content

Role	**Name**	**Chemistry (wt%)[1]**			
		C	**H**	**O**	**N**
MA	Ti6Al-MA-coarse	0.062	0.020	0.295	0.388
MA	TiAl-MA-fine	0.041	0.014	0.453	0.132
BE	Ti6Al-BE-coarse	0.010	0.012	0.176	0.010
BE	Ti6Al-BE-fine	0.010	0.012	0.201	0.010

[1]Refer to Appendix C

3.2 Compact Preparation

Powder blends were placed into a cylindrical cavity of 4.83 mm in diameter for DSC tests and 6.35 mm in diameter for dilatometer tests. The die walls were coated with lubricant wax before the powder was placed into the cavity. The depth of the cylindrical dies was mechanically controlled. The powder was poured into the cavity, and the excess powder was scraped away creating a full and uniformly filled die cavity. For the DSC die this resulted in an average mass of 70.79 mg for DSC compacts and 163.95 mg for dilatometer compacts.

Table 7 DSC and DIL compact characteristics

	DSC			DIL		
	Mass (mg)	**Diameter (mm)**	**Thickness (mm)**	**Mass (mg)**	**Diameter (mm)**	**Thickness (mm)**
Average	70.79	4.83	1.03	1163.95	6.37	10.23
Stdv	4.25	0.01	0.08	35.10	0.01	0.52
% diff	6.0%	0.2%	7.4%	3.0%	0.2%	5.1%

The powder was uniaxially pressed between hardened steel punches in a Carver hand press. The force, 15 700 N for the small DSC compacts and 19 600 N for the larger dilatometer compacts, was reached at a constant rate and held for 10 seconds. The force applied represents 856 MPa for the DSC compacts and 620 MPa for the dilatometer compacts. The compacts were then ejected from the dies. The wall friction caused the compacts to display a raised edge or flashing. This edge would prevent the compact from sitting perfectly flat in the crucible. Thus, it was removed using a sharp scalpel. Estimates of the pressed green density based on the weight and dimensions of the sample were 3.73 g/cm^3 for DSC samples and 3.58 g/cm^3 for the dilatometer samples.

3.3 Differential Scanning Calorimetry

Compacts were sintered in the DSC furnace in a pure Argon (99.999%) atmosphere with a constant flow rate of 50 ml/min and normally heated up to 1200˚C at 20˚C/min and cooled down at 40˚C/min. Figure 22 presents the normal temperature profile (solid line) for the DSC analysis. The hold time at 1200°C (i.e. sintering time) was varied from 0 to 120 minutes for different samples. In some cases samples were heated to a peak temperature below 1200°C and rapidly cooled at 100°C/min. in order to observe the microstructure developed in the compacts as a function of temperature.

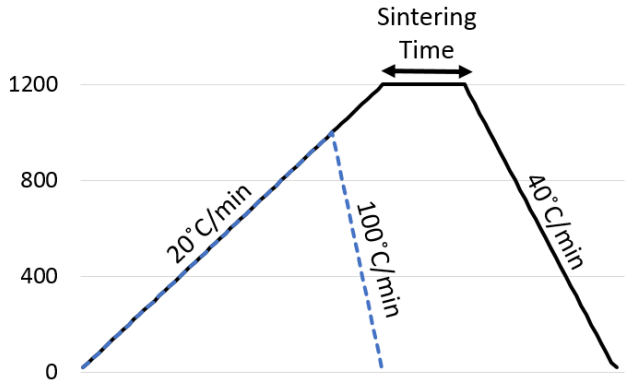

Figure 22 Temperature profiles used for the sintering in the DSC

Although most DSC tests are done using an alumina (Aluminum oxide) crucible, the compacts were placed in a crucible made from yttria (yttrium oxide) to minimize the possible contamination between the Titanium powder blends and the crucible. The crucible was periodically baked out in air to remove any contaminants stuck on it. The reference crucible is an empty alumina crucible of the same dimension as the yttria crucible.

Six metallic standards (In, Bi, Sn, Al, Ag and Au) were used to calibrate the DSC temperature and sensitivity. The DSC trace analyses were done using Netzsch Proteus 6.1 software [48].

3.4 Dilatometry

The compacts were heated in a DIL furnace at a rate of 20°C/min from 150°C to the sintering temperature of 1200°C and were held at 1200°C for one hour. Protective alumina plates were covered with a yttria coating and placed at both ends of the compacts. The sintering was completed under full vacuum. The furnace chamber was purged with Argon twice before the cycle started, ensuring that no Oxygen or other impurities were present during sintering at high temperature. Figure 23 presents the Netzsch DIL 402C similar to the model used to perform the study.

Figure 23 Dilatometer Netzsch DIL 402 C

Similarly to DSC analysis, DIL traces were analyzed using Netzsch Proteus 6.1 software [48].

3.5 Microscopy Analysis

Microscopy analysis was done to observe the compact microstructure and porosity. DSC compacts were mounted in epoxy resin and polished to a mirror finish. Samples were then etched with Kroll's reagent. The samples were observed under an Olympus optical microscope binocular, using Fiji ImageJ2 [49] for image analysis, or under a Hitachi S-4700 Field Emission Scanning Electron Microscope, with back scattered electrons, managed by the Institute for Research in Materials [50].

Chapter 4. Results and Discussion

The present chapter outlines the observations made in terms of comparing the influence of starting powder type and size on the processing of the Titanium Aluminum formulations. The chemical homogenization response of the powder blends was analyzed using DSC and associated microstructural analysis. There were two stages in the DSC homogenization analysis: heating and cooling. Both present different aspects of the alloying and sintering characteristics of each blend, and were monitored according to the powder source and powder size of the additions. The densification behavior was independently analyzed using high-temperature dilatometry.

4.1 Initial Heating Behaviour

4.1.1 Heating Behaviour of Commercially Pure Titanium Powder Compacts

Figure 24 presents the heating thermograph of a powder compact of elemental CP-Ti. The trace is from the heating stage and the endothermic peak is representing the α-β phase transformation. The area under the peak represents the enthalpy of the transformation and can be measured using the DSC analysis tools package.

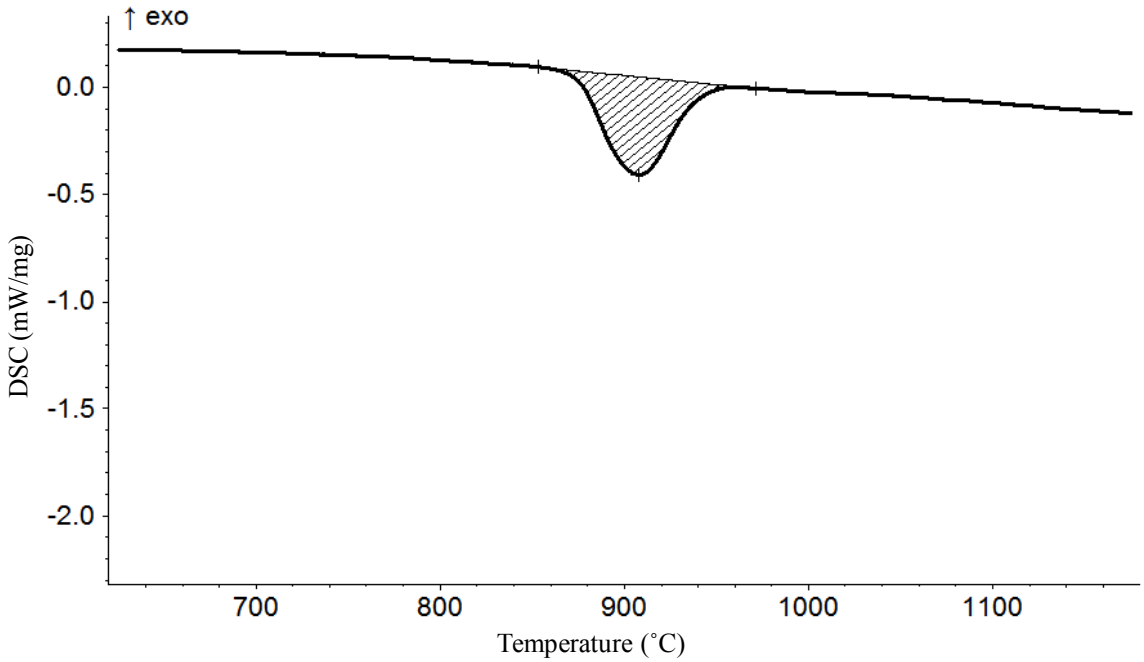

Figure 24 Heating trace of a CP-Ti compact, heated up to 1200°C at 20°C/min

The onset temperature was measured to be 874 ± 2°C and the enthalpy was measured as 60.5 ± 1.6 J/g.

The measured onset temperature is lower than the 882°C α-to-β phase transformation onset point predicted by Figure 9. This is likely due to small levels of impurities present in the CP-Ti powder. DSC traces of CP-Ti will be used as the baseline, and 874.1°C will be used as a reference temperature to assess the effect of the alloying addition on the α-to-β phase transformation onset point.

4.1.2 Heating Behaviour of Titanium-6Aluminum Powder Compacts

Figure 25 plots the heating traces for the four Ti6Al powder mixtures. The Ti6Al-BE mixtures, on Figure 25 (a), show an exothermic shift in the baseline with a preliminary onset temperature at 546.7°C for Ti6Al-BE-fine and at 553.7°C for Ti6Al-BE-coarse. At a temperature of 654.7°C and 658.0°C, for the fine and coarse Ti6Al mixtures respectively, there is a sharp exothermic peak, which ends just below 700°C. The Ti6Al-MA mixtures show no evidence of any thermal events in the temperature range of 500 to 700°C (see Figure 25 (b)).

Like the CP-Ti of Figure 24, all powder blend compacts of Figure 25 go through the α-to-β transformation with an onset temperature of about 873°C. It is interesting to note that even though the transformation starts at the same temperature, the enthalpy of the transformation is significantly less for the Ti6Al blends compared to the CP-Ti compacts, as presented in Table 8.

Part of the reason for this lower enthalpy is due to the lower mass percentage of CP-Ti in the compact available for the phase transformation in the Ti6Al compacts than for the CP-Ti compacts. To calculate the theoretical enthalpy values of each powder source, it is assumed that there is no diffusion of Aluminum before the α-to-β onset temperature. In that situation, Ti6Al-BE containing only 94% CP-Ti powder should exhibit an enthalpy 94% of the CP-Ti value from section 4.1.1, resulting to 56.6 J/g, because pure Aluminum would not contribute to the transformation. Ti6Al-MA contains only 83% of CP-Ti powder, the theoretical enthalpy of the MA mixture should be 50.2 J/g, because the intermetallic TiAl, like the pure Aluminum, would not contribute to the enthalpy.

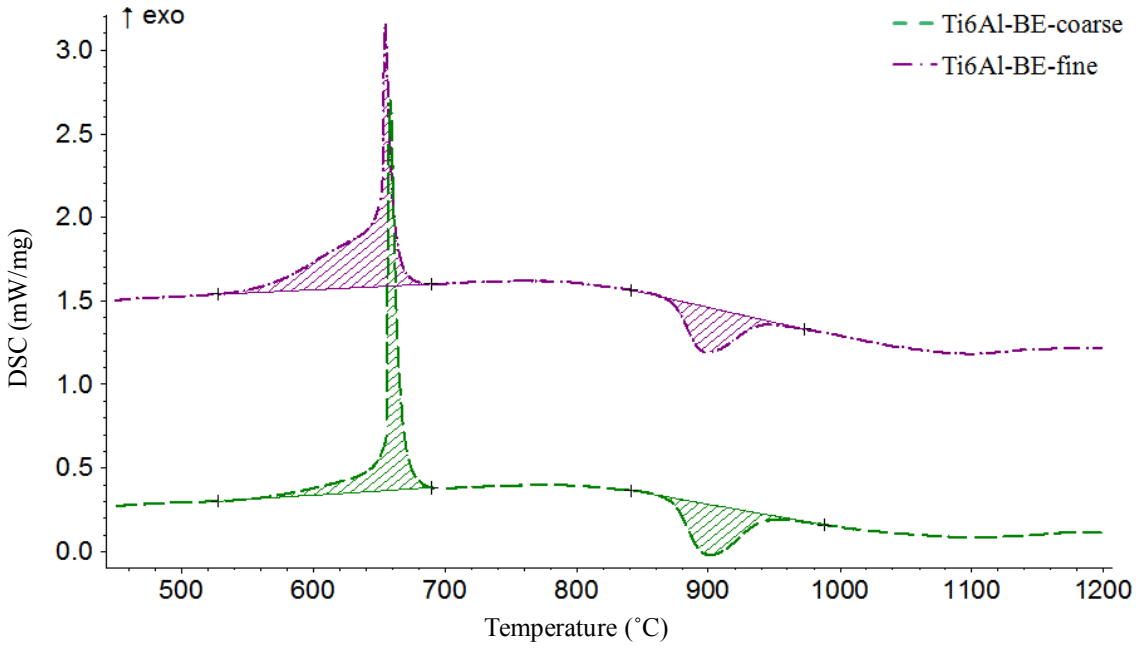

(a)

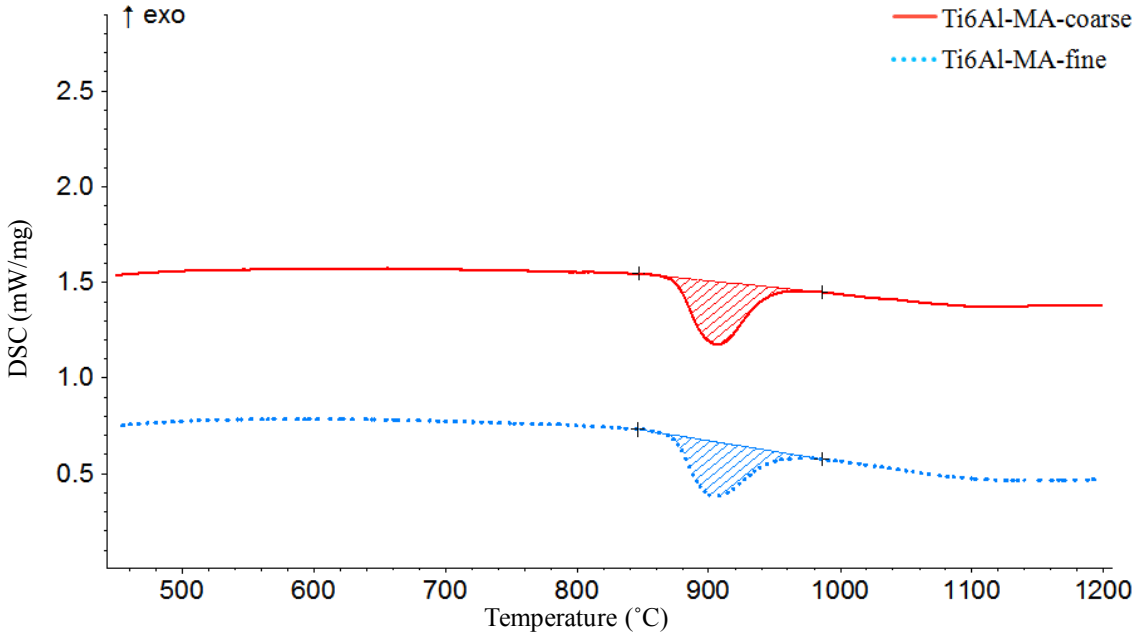

(b)

Figure 25 Thermographs of the various powder blend compacts during heating (a) blended elemental compacts and (b) master alloy compacts

Table 8 Endothermic peak of the different powder blends during heating

	Onset T° (°C)	STDEV (°C)	Enthalpy (J/g)	STDEV (J/g)
Ti6Al-MA-coarse	873.3	1.8	43.5	3.6
Ti6Al-MA-fine	871.4	2.1	35.8	3.2
Ti6Al-BE-coarse	873.2	0.3	44.2	4.2
Ti6Al-BE-fine	872.7	0.6	33.7	0.8

The onset temperature of the α-to-β phase transformation is 872.7°C ± 1.6°C and was calculated with more than 10 different samples. Comparing the theoretical values for enthalpy to the measured ones from Table 8 exhibits disagreement. This is due to the simplifying assumption that no interaction between the BE and MA particles and the CP-Ti occurs during heating. In order to understand the DSC measurements better and their comparison with the theoretical calculations, microstructural examination of the samples was performed.

4.1.3 Microscopy Analysis of the Samples During Heating

In order to better understand the thermal events indicated by the DSC trace in the range of 500 to 700°C, several pressed compacts of the Ti-6Al coarse MA blends were interrupted in the heating phase of their sintering. Figure 26 presents Ti6Al-BE-coarse compacts which were heated up to temperature below the peak observed on Figure 25, at 645°C and above the melting point, at 680°C, to observe the behaviour of the Aluminum.

At 645°C, there are still pockets of pure Aluminum which are identifiable due to their bright white contrast after etching. Close examination indicates that a thin grey boundary has locally developed on the surface of the Ti powders that are in direct contact with the Al particles. This microstructural evidence indicates that there is a solid-state reaction between the Aluminum and the Titanium matrix. The DSC indicates that this begins to occur at 546.7 and 553.7°C for the fine and coarse BE blends respectively. The sample cooled from 680°C (Figure 26 c) indicates large pores where the Al particles were located at 645°C. In addition, nearly all of the Ti particles surfaces are now covered with an intermetallic layer. The large exothermic reaction which onsets above 654.7°C, measured

in the DSC, supports this microstructural change. Specifically, the microstructural evidence of Figure 26 confirms that this exothermic reaction initiates when the Al melts and spreads throughout the Ti powder compact. The magnitude of this exotherm hides the endothermic melting of Aluminum that would otherwise be seen on the DSC trace.

Overall the onset temperature and extent of exothermic reaction both in the solid and liquid state are influenced by the size of the Al BE particles added to the mixture. According to the DSC analysis of Figure 25 (a), a fine particle size promotes a more extensive intermetallic reaction (ΔH_{exo} = 89.93 J/g) which begins at lower temperatures compared to the coarse BE mixtures with an exothermic reaction of 74.33 J/g.

In order to better understand the influence of Al additions of the α-to-β phase transformation, Figure 27 and Figure 28 compare the microstructural evolution at 850°C, 950°C and 1050°C for the Ti6Al mixtures made using coarse pure Aluminum and master alloy additions during the heating stage. Coarse powder additions were selected because they show the process better due to their slower interaction. The temperature chosen, 850°C, 950°C and 1050°C are respectively at the beginning, the middle and the end of the α-β phase transformation exhibited in the DSC trace.

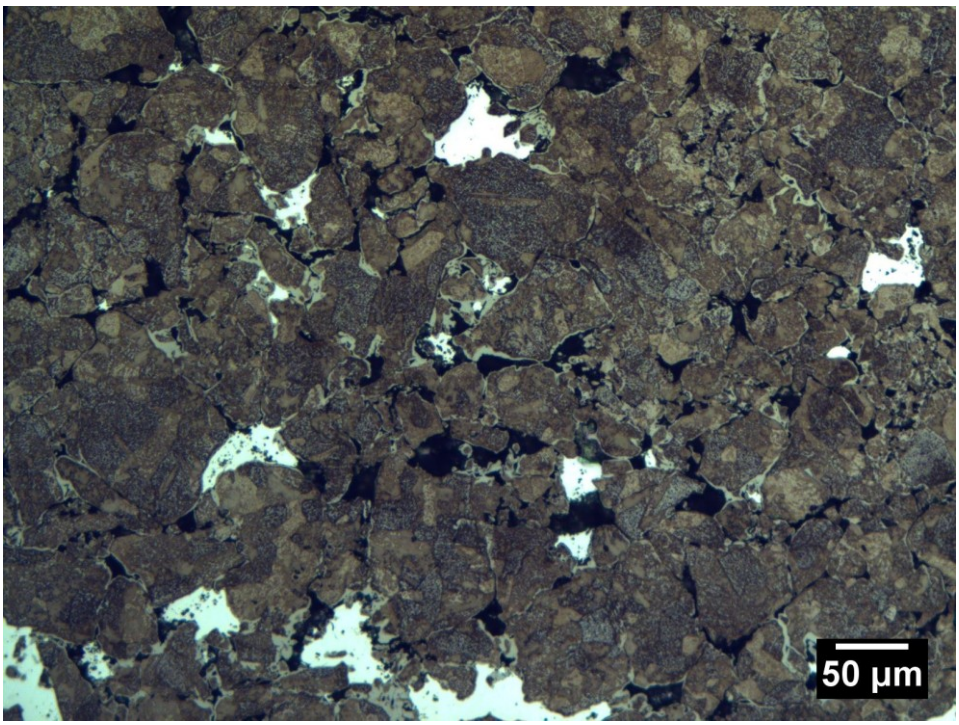

(a)

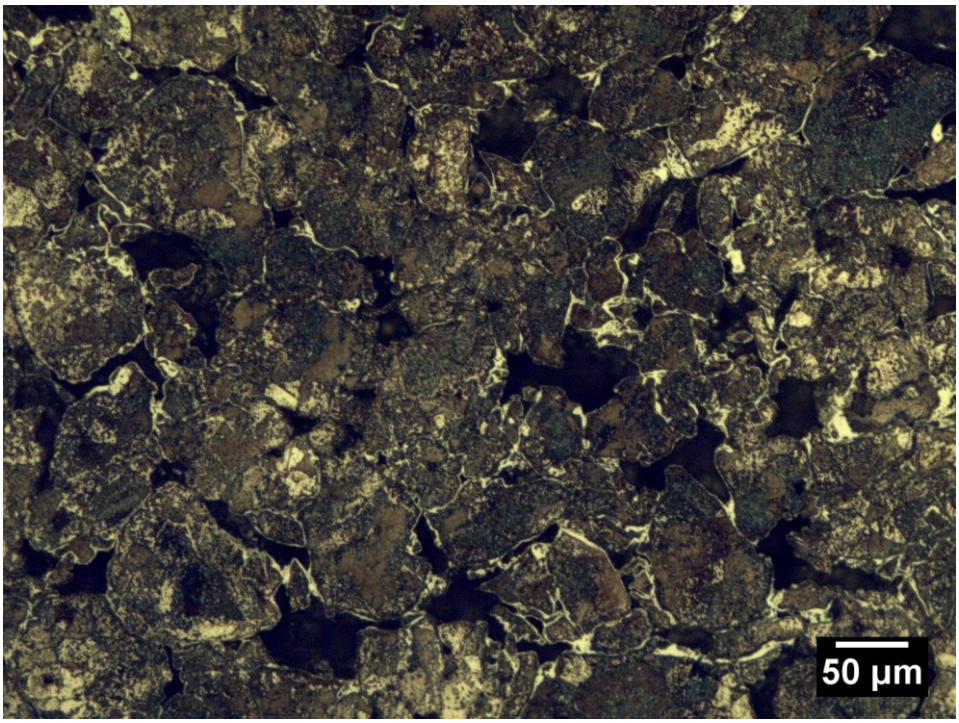

(b)

Figure 26 Microstructure of a coarse BE Ti-6Al compact heated up at 20°C/min and rapidly cooled down at 100°C/min): (a) 645°C and (b) 680°C.

On Figure 27 (a), Ti6Al-BE-coarse at 850°C looks similar to the 680°C of Figure 26 (c) with CP-Ti particles surrounded by a very thin grey Aluminum-Titanium intermetallic region. This Aluminum-rich boundary is growing in thickness at the particle surface with the increase in temperature (Figure 27 (a), (b) and (c)).

The microstructure of the Ti6Al-MA-coarse sample is evolving much differently than Ti6Al-BE-coarse, as evidenced in Figure 28 (a), (b) and (c). At 850°C, there is no evidence of interaction between the CP-Ti and MA particles. There is a complete absence of a network of Ti-Aluminide intermetallic boundaries around the CP-Ti particles. This is due to the fact that the TiAl MA particles do not undergo melting and spreading like BE Al does. This lack of melting and spreading is supported by the DSC traces for the MA blends, since no exothermic reactions occurred in the range of 500°C to 700°C. At 950°C a bright white layer begins to develop at some contact points between the CP-Ti and MA particles. The master alloy particles are recognisable by their size and by their microstructure even at 1050°C. The bright white layer is visible all around the coarse MA particles where they contact the CP-Ti, which may be the formation of a Ti_3Al layer around the TiAl particle or a Ti rich solid solution layer. It is interesting to note that, in contrast to the coarse BE Ti6Al sample of Figure 27c), no continuous layer of intermetallic has developed around CP-Ti powders that are not in contact with a MA particle.

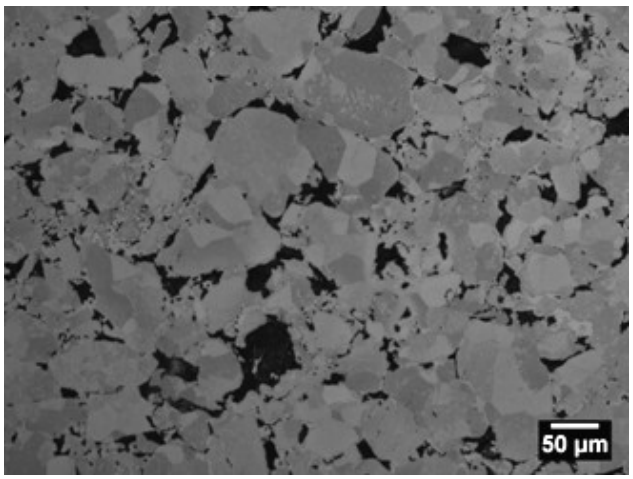

(a)

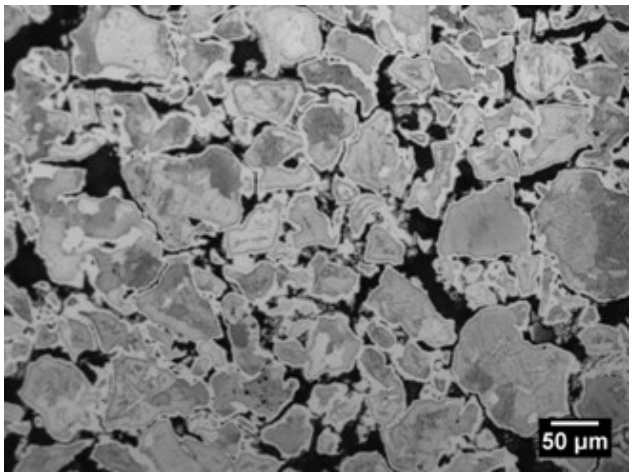

(b)

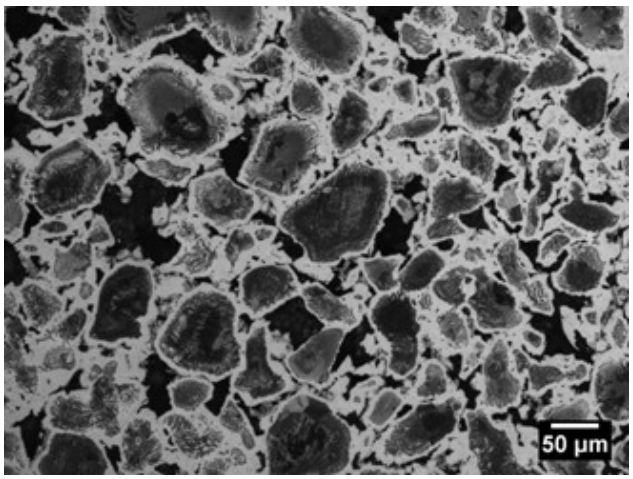

(c)

Figure 27 Microstructure of Ti6Al-BE-coarse at (a) 850°C, (b) 950°C and (c) 1050°C, (heated up at 20°C/min and rapidly cooled down at 100°C/min)

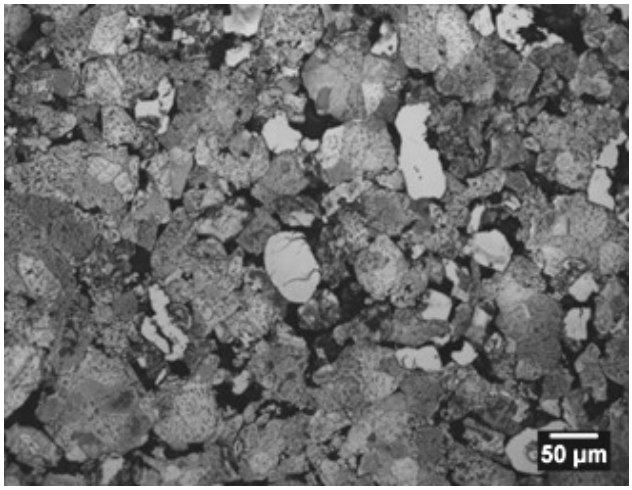

(a)

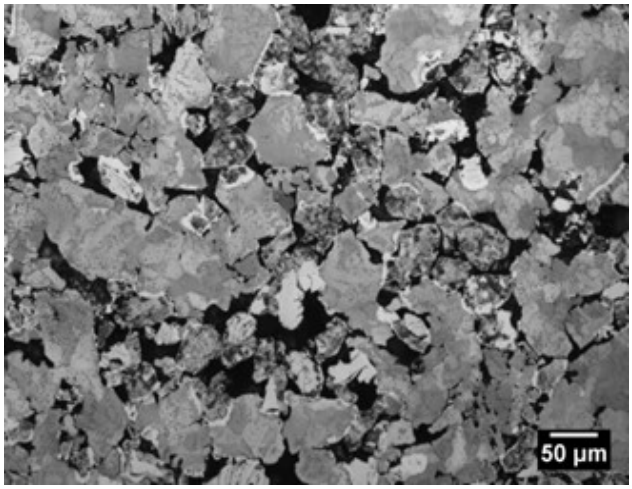

(b)

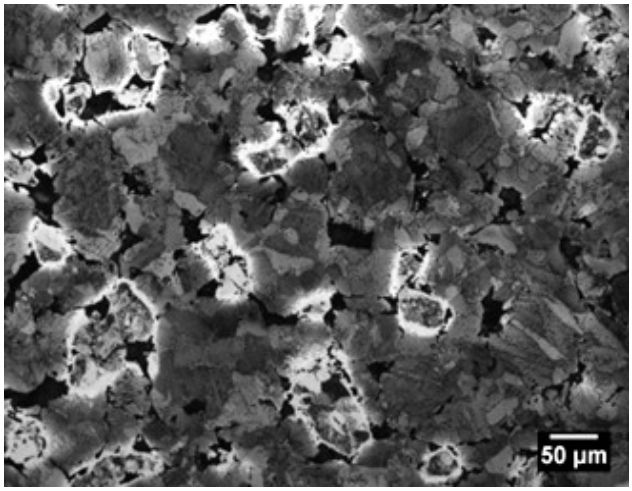

(c)

Figure 28 Microstructure of Ti6Al-MA-coarse at (a) 850°C, (b) 950°C and (c) 1050°C (heated up at 20°C/min and rapidly cooled down at 100°C/min)

With the above microstructural evidence, it is now possible to interpret the DSC results presented in Table 8. For the Ti6Al-BE-coarse blend the $\Delta H_{\alpha-\beta}$ is 44.2 J/g, which is 12.4 J/g less than the theoretical value calculated previously. Figure 27a) indicates that this is due to the consumption of some of the Ti to form Aluminum-Titanium intermetallics. In the case of Ti6Al-BE-fine, the difference is 22.9 J/g which indicates that even more of the Ti is consumed through the formation of intermetallics. This was confirmed through examination of the Ti6Al-BE-fine mixtures (not shown). The surface area of the fine Aluminum powder additions and its contact with the Ti powder is much higher than that of the coarse Al powder, leading to more reaction with Ti. As shown on Figure 9, only α-Titanium undergoes the α-to-β phase transformation at a single temperature. The intermetallics formed by the rapid diffusion of Aluminum in the CP-Ti matrix do not undergo a phase transformation in this temperature range.

In the case of the MA Ti6Al blends, the microstructure of Figure 28 a) shows much less interaction with the Ti matrix, largely due to the fact that the Al is already combined into an intermetallic and did not melt and spread through the powder mixture. This results in a measured $\Delta H_{\alpha-\beta}$ that is close to the theoretical value of 50.2 J/g for the MA blends (i.e. 33.7 and 44.2 J/g for the fine MA and coarse MA blends respectively). Small deviations less than the theoretical are likely due to the consumption of the pure Ti to form the more Ti rich Ti_3Al at the TiAl MA particle surface. There is more consumption of the pure Titanium with the Ti6Al-MA-fine blend than with the Ti6Al-MA-coarse, because there is more surface in contact between the fine MA particles and the CP-Ti than with the coarse particles. This is shown on Figure 29 (a) for coarse particles and (c) for fine particles.

Figure 29 helps to compare and summarise the heating stage of sintering and the influence of type and size of Al containing powder addition. In the case of the BE mixtures, Aluminum reacts both in the solid-state and during melting to form Ti-Aluminide intermetallics at the CP-Ti particle surface. The melting process in particular, distributes the Al much faster with the blended elemental additions compared to the MA additions, due to the exothermic reaction that distributes a thin layer of Aluminum throughout the matrix during which the intermetallic boundary is formed. With further heating above 680°C, the intermetallic layer grows in thickness and the Al begins to

diffuse into the interior of the Ti particles. This is most evident in the fine BE blend of Figure 29 (d), where a platelet like structure typical of a Ti rich Ti-Al solid solution begins to form. Overall the fine BE compact indicates more interdiffusion than the coarse BE blend at 1050°C. For example, the darkly etched regions of Figure 29 indicate unalloyed CP-Ti regions which represent a higher volume fraction in the coarse BE blend compared to the fine BE blend.

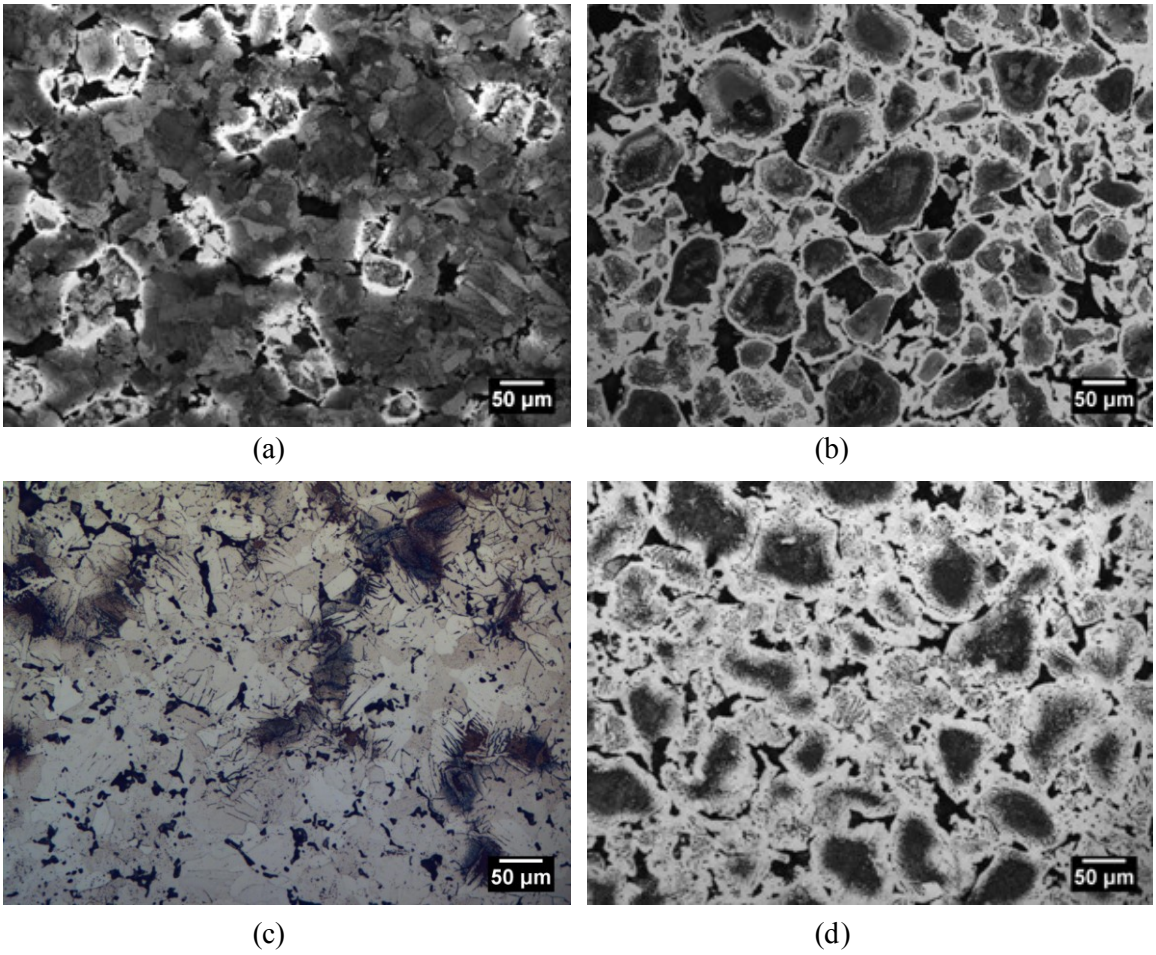

(a) (b)

(c) (d)

Figure 29 Comparison between the compacts' microstructure after being heated up at 1050°C at 20°C/min and rapidly cooled down at room temperature at 100°C/min: (a) Ti6Al-MA-coarse, (b) Ti6Al-BE-coarse, (c) Ti6Al-MA-fine and (d) Ti6Al-BE-fine

The master alloy particles are stable, do not melt, do not create any exothermic reaction and as a result are slower to distribute into the matrix. The coarse MA Ti6Al blend at 1050°C indicates the least amount of interaction and a very high volume fraction of

darkly etched, unalloyed CP-Ti at 1050°C. Conversely, the use of fine MA particles has greatly accelerated interaction and produced very low levels of unalloyed Ti regions at 1050°C.

4.2 Cooling Behaviour

In section 0, the focus was on the heating phase of sintering, the first step to understanding the effect of each powder source. The results indicate that many of the mixtures remain inhomogeneous to various degrees after heating to 1050°C. Different sintering times would not affect the heating phase but should have a strong impact on the degrees of homogenization that should occur. This section will go over the full range of sintering time, starting at no hold time and finishing with a time required to fully homogenize the compact. Similarly to section 0, the study will be focused on DSC analysis and the comparison of the different microstructures of each powder blend.

4.2.1 Cooling Behaviour of Commercially Pure Titanium

In a previous study by Steedman and Corbin [39], a technique was developed using DSC to measure the degree of homogenization in α/β alloys. The technique is based on the fact that the β-to-α phase transformation during cooling is very sensitive to the composition of the alloy.

The temperature of the β-to-α transition recorded by DSC can be used as an indication of the alloying state since alloying additions affect the thermograph profile, shifting the cooling phase transformation peak temperature and height and shifting the onset and end points, which modifies the area under the curve. The width of the temperature range over which the β-to-α transition occurs is an indication of the homogeneity of the compact. Aluminum rich regions tend to stabilize more α-phase, thus transitioning back from β-to-α at a much higher temperature (1100°C) with 6 wt % of Al than CP-Ti (882°C) as presented in Figure 9. Width, starting and ending temperature of the DSC peak are useful information to compare the homogeneity in a compact when comparing the different sintering states or to CP-Ti.

The extent to which the alloying element remains separated from the matrix can be monitored by using CP-Ti as the reference. Figure 30 presents the cooling trace of CP-Ti. It shows that the β-to-α transformation starts at 934.9°C, with its peak being at 874.5°C, and ends at 848.7°C at a cooling rate of 40°C/min.

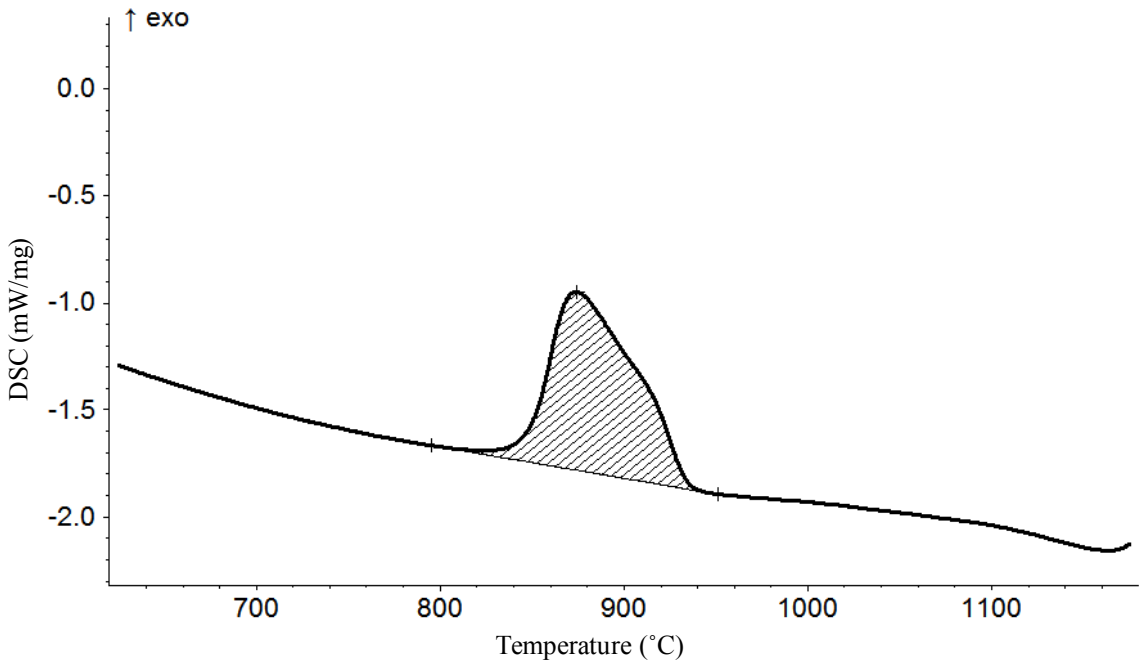

Figure 30 Cooling trace of a CP-Ti compact heated up to 1200°C at 20°C/min and cooled down to room temperature at 40°C/min

4.2.2 Calorimetry Analysis of the Titanium-6Aluminum Powder Compacts

Figure 31 presents the cooling traces of the different powder blends after the compacts were heated up to 1200°C at 20°C/min and cooled down to room temperature at 40°C/min.

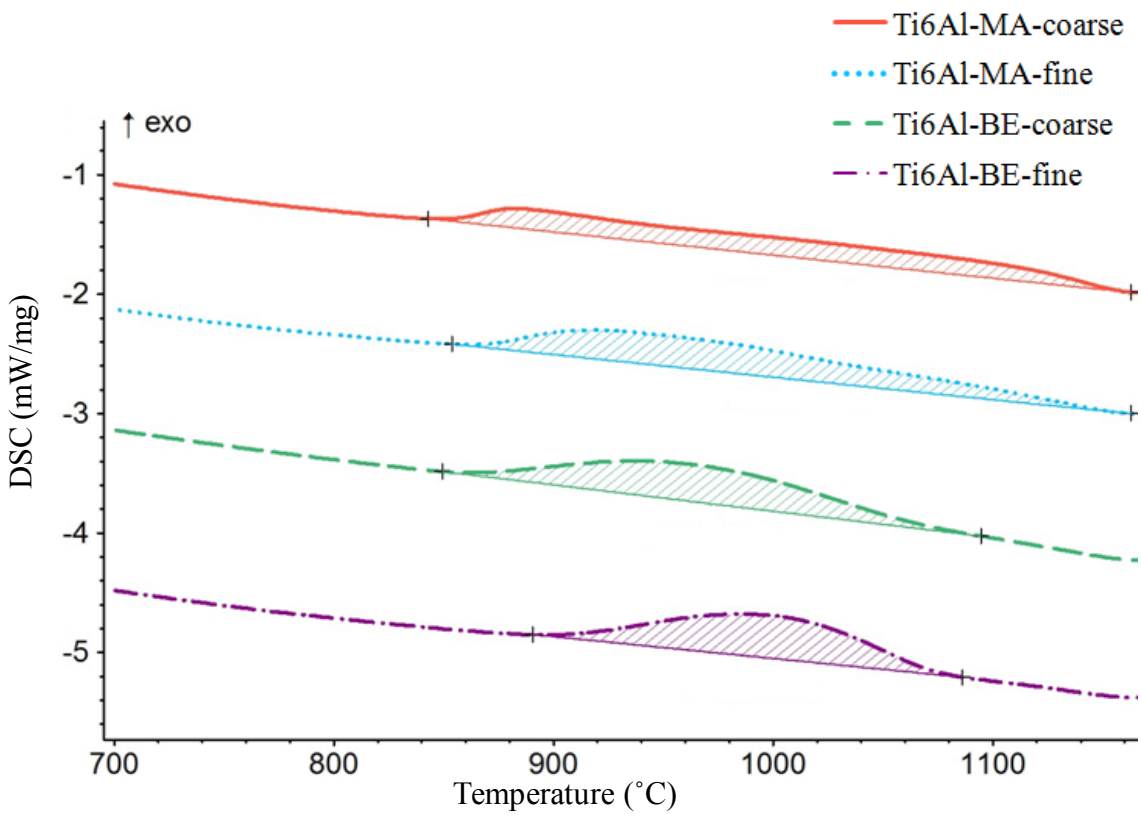

Figure 31 Cooling traces of the different powder blends after the compacts were heated up to 1200˚C

Ti6Al-MA blends generate a significantly broader β-to-α transition than Ti6Al-BE blends for both powder size ranges. The beta transus (i.e. the temperature at which the alpha phase begins to form during cooling) also occurs at a higher temperature in the MA blends. All blends have a beta transus above the CP-Ti powder compact. The beta transus temperature is an indication of the local alloying percentage and the width of the temperature range over which the β-to-α transition occurs is an indication of the homogeneity of the compact. For example, Aluminum rich regions tend to stabilize more α-phase, thus creating a higher β transus. Ti6Al-MA-coarse presents a noticeable peak height around the CP-Ti transformation temperature (i.e. 880°C), which indicates that a portion of the microstructure is still nearly pure CP-Ti and Aluminum poor. Comparatively, Ti6Al-BE-fine presents a relatively sharp and narrow phase transformation peak, which indicates a much better homogenization of the Aluminum in the matrix.

As shown in Figure 31, each powder source and size are behaving differently after no hold time when sintering at 1200°C. The next sections will take a closer look at the sintering behaviour of each powder blend as the sintering time is increased.

4.2.2.1 Cooling thermographs of Ti6Al-BE-fine after different sintering times

Figure 32 presents the endothermic traces generated by the sintering of Ti6Al-BE-fine at 1200°C for no hold time, 15 minutes, 30 minutes, 45 minutes, 60 minutes and full homogenization. Full homogenization was achieved by sintering each powder blend for 120 minutes at 1200°C and then successively cooling them down to 20°C and heating them back to 1200°C three times. Appendix D presents the results of these successive cycles for each powder blend. The variation between the successive cycles after full homogenization is less than 5% for every powder blend, as presented in Table 18 from Appendix D. The DSC cooling curve labeled as "homogenized" in Figure 32 is the last cooling segment after the 3 cycle homogenization process described above.

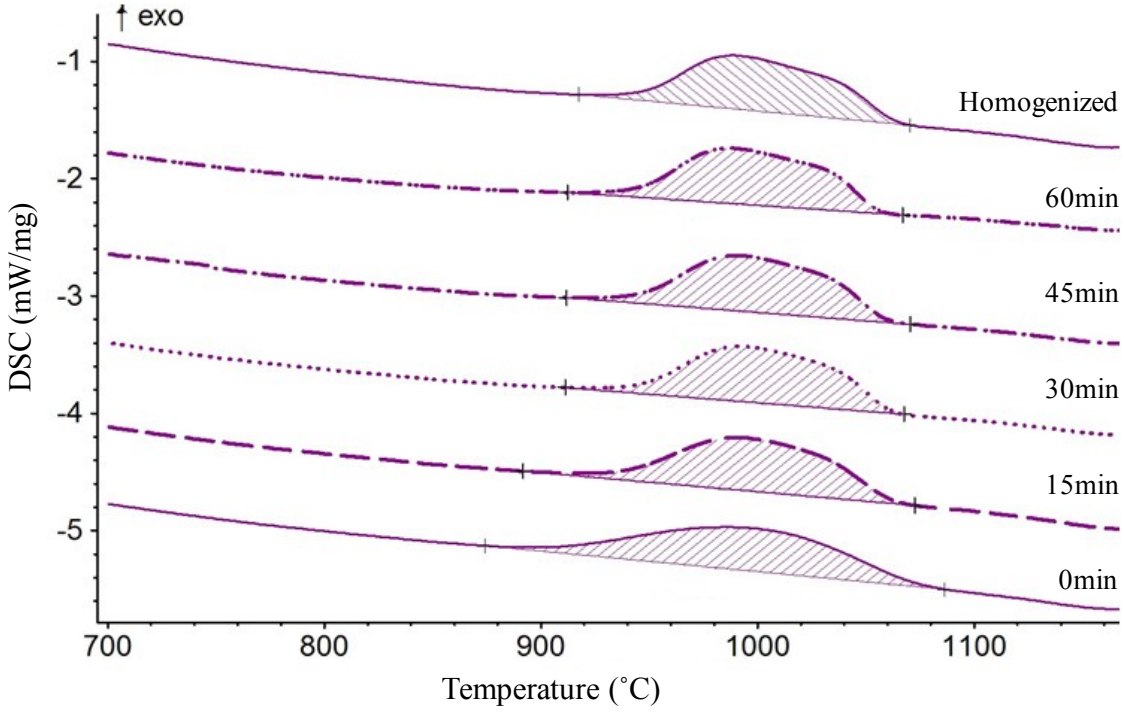

Figure 32 Cooling thermograph traces of Ti6Al-BE-fine after being held at 1200°C for various hold time

A number of measurements can be obtained from β-to-α phase transformation peaks of Figure 32. These include the areas under the peak in J/g (or the enthalpy of the transformation), the temperature at which the maximum peak height occurs in °C (i.e. Peak Temperature), the peak width at 50% of the maximum peak height in °C and the maximum peak height in mW/mg. A summary of all these measurements is presented in Table 9.

Table 9 Exothermic peak characteristics of the sintering of Ti6Al-BE-fine at different sintering time during the cooling phase

		Enthalpy (J/g)	**Peak (°C)**	**Width 50% (°C)**	**Height (mW/mg)**
Ti6Al-BE-fine	**0 min**	59.03	998.7	107.1	0.3647
	15 min	57.91	995.6	85.5	0.4486
	30 min	57.28	995.0	82.1	0.4717
	45 min	56.81	993.9	81.0	0.4735
	60 min	56.02	989.7	81.1	0.4719
	Homo	56.5	994	84	0.444

The peak temperature is shifting to lower values as the sintering time increases and is stabilizing at 994°C. The peak width also narrows with increase time around this temperature, ranging from a width of 107.1°C with no hold time to 84°C at the fully homogenized stage.

4.2.2.2 Cooling thermographs of Ti6Al-BE-coarse after different sintering times

Figure 33 presents the endothermic traces generated by the cooling stage of Ti6Al-BE-coarse sintered at 1200°C for no hold time, 15 minutes, 30 minutes, 45 minutes, 60 minutes and full homogenization.

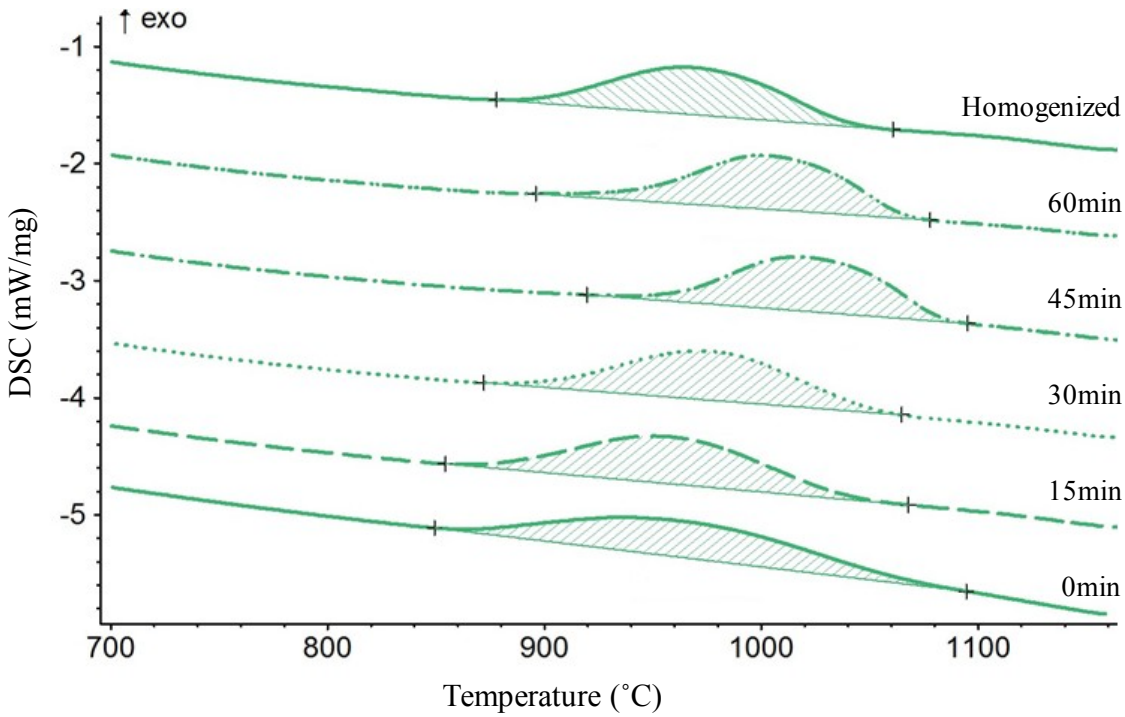

Figure 33 Cooling traces of Ti6Al-BE-coarse after being held at 1200°C for various hold time

As the sintering time increases in Figure 33, the peak temperature is shifting, first to higher α-to-β transformation temperature and then is stabilizing back down at 968°C, as presented in Table 10. The peak width also narrows as sintering time increases, starting at 129.7°C, with no hold time, to 87°C at the fully homogenized state.

Table 10 Exothermic peak characteristics of the sintering of Ti6Al-BE-coarse at different sintering time during the cooling phase

		Enthalpy (J/g)	**Peak (°C)**	**Width 50% (°C)**	**Height (mW/mg)**
Ti6Al-BE-coarse	**0 min**	60.52	963.7	129.7	0.3104
	15 min	60.24	958.3	97.6	0.4011
	30 min	58.37	977.8	90.4	0.4174
	45 min	57.26	1020.0	81.2	0.4620
	60 min	57.69	1003.8	80.4	0.4586
	Homo	56.0	968	87	0.421

There is more shifting in the peak temperature in Figure 33 than there is with Ti6Al-BE-fine in Figure 32. Both are blended elemental compacts, but the particle size of the pure

Aluminum addition is affecting the homogenization response. It takes more sintering time for coarse Aluminum powder to fully diffuse into the matrix than it does for fine powder.

4.2.2.3 Cooling thermographs of Ti6Al-MA-fine after different sintering times

Figure 34 presents the cooling phase transformation behaviour of Ti6Al-MA-fine after sintering for various hold times. With no hold time, the peak of the β-to-α phase transformation is at 948°C and it shifts up to 1042.5°C after sintering for only 15 minutes, which indicates that a higher percentage of the mass is containing a high Aluminum percentage. The Aluminum-rich regions are transforming back at a high onset temperature and the phase transformation occurs at much lower temperature in Aluminum-poor areas. When the two regions are present in the compact, before chemical homogenization, the β-to-α exothermic peak is broad.

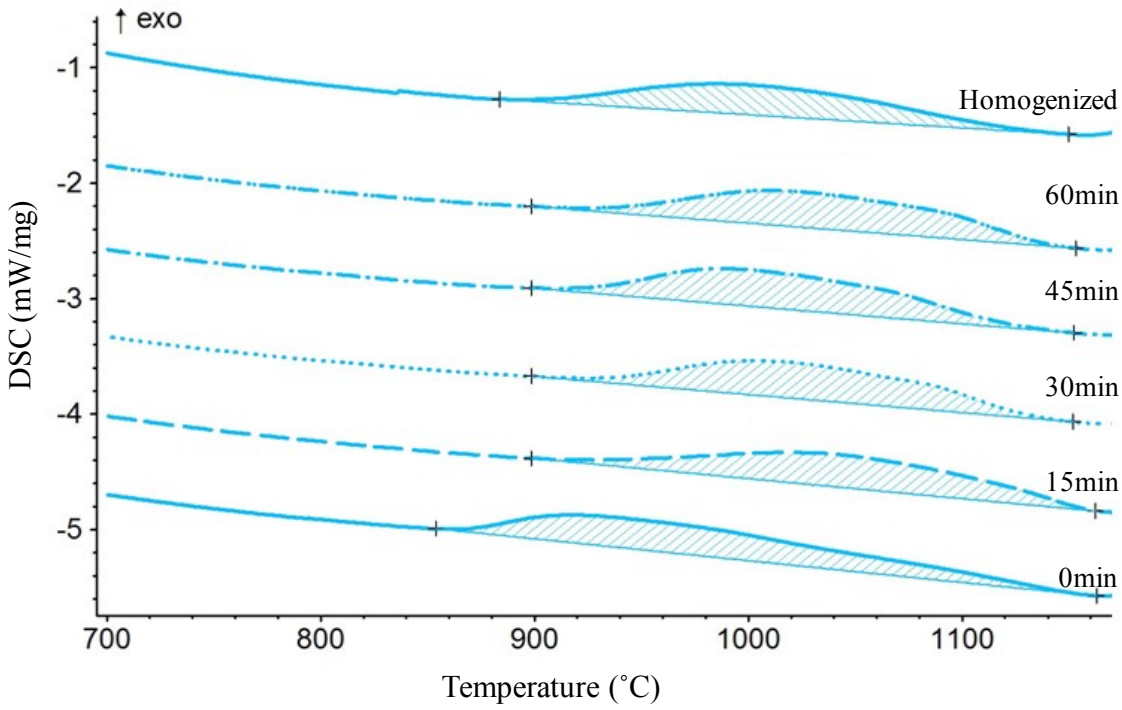

Figure 34 Cooling thermograph traces for Ti6Al-MA-fine after being held at 1200°C for various hold times

The most noticeable feature of the traces is how broad they are. Even a fully sintered Ti6Al-MA-compact transforms back from β-to-α over 134°C, which is a lot broader than any of the Ti6Al-BE compacts. The peak temperature of the β-to-α phase transformation

is shifting a lot, but since the height is very low, it does not appear to be a clear indication of the chemical homogeneity within the compact. The values of the peak's characteristics are presented in Table 11.

Table 11 Exothermic peak characteristics of the sintering of Ti6Al-MA-fine at different sintering time during the cooling phase

		Enthalpy (J/g)	Peak (°C)	Width 50% (°C)	Height (mW/mg)
Ti6Al-MA-fine	**0 min**	68.24	948.5	179.9	0.258
	15 min	61.97	1042.5	149.2	0.2824
	30 min	62.32	1015.9	136.7	0.3119
	45 min	63.46	1004.0	134.7	0.3164
	60 min	63.67	1023.9	141.1	0.3074
	Homo	52.4	998	134	0.261

As presented in Table 5, Ti6Al-MA-fine has the highest Oxygen impurity content and the second highest Nitrogen impurity content among the different powder additions. Oxygen and Nitrogen are α-stabilizer additions, and as little as the 0.453% of Oxygen present in this Ti6Al-MA-fine is sufficient to affect the β-to-α phase transformation by increasing it, as presented in section 1.3. The peak temperature and onset temperature are affected by the inhomogeneity with the Aluminum content as well as with the impurities present in the compact.

The enthalpy of the β-to-α transformation in Ti6Al-MA-fine at 0 min is very close to CP-Ti but gets smaller with increased sintering time. The reason for this variation in enthalpy is related to the degree of retained beta at room temperature. For example Malinov et al. [51] used XRD to point out the retained beta is a common feature in wrought Ti6Al4V. Recently, Steedman and Corbin [39] have used both DSC and XRD to show that the magnitude of the β-to-α transformation enthalpy is directly related to the presence of retained beta in sintered Ti6Al4V blends. Specifically, Ti6Al4V blends that exhibited an enthalpy close to 70 J/g showed no retained β in their XRD spectrum while samples with enthalpies close to 50 J/g did. A similar process is proposed to operate in the Ti-6Al blends of this study.

4.2.2.4 Cooling thermographs of Ti6Al-MA-coarse after different sintering times

Figure 35 presents the cooling traces of the Ti6Al-MA coarse that were sintered for various hold times. For the Ti6Al-MA-coarse blend, the exothermic peak is broad. At 0 minutes, the major peak temperature is at 892.7°C, but there is a second peak around 1080°C, likely due to the inhomogeneity of the Aluminum distribution within the compact. The Aluminum rich zone β-to-α phase transformation is occurring at a higher temperature than the Aluminum poor zone, which would occur closer to 882°C, as presented on Figure 30.

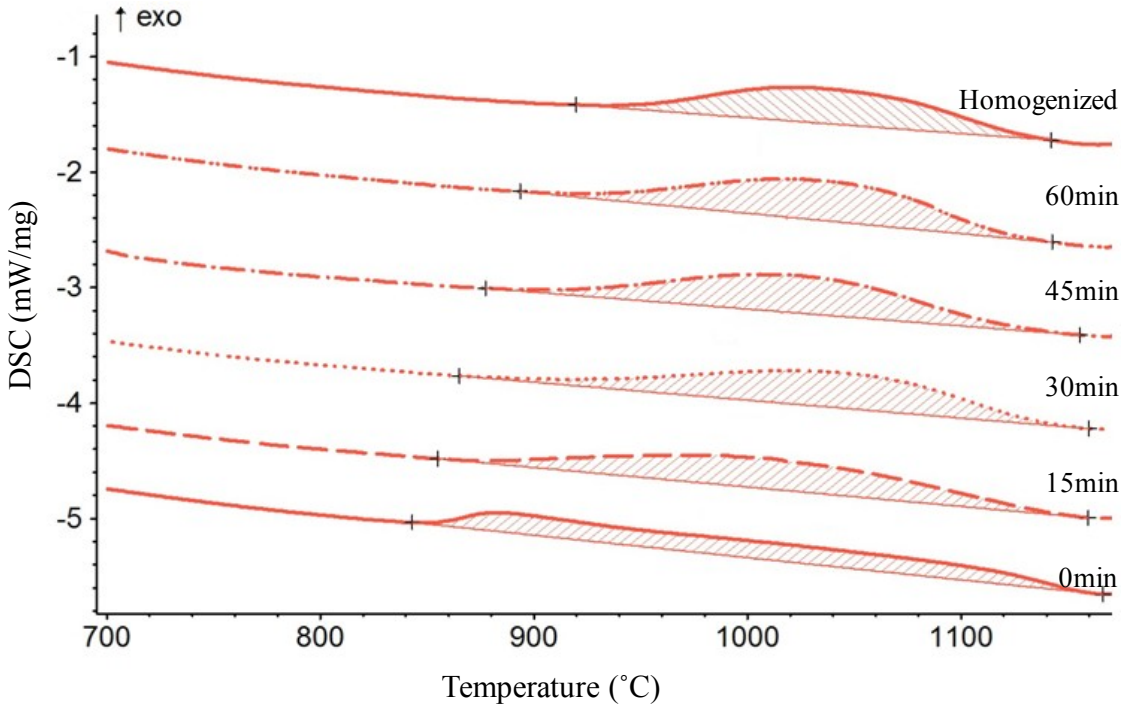

Figure 35 Cooling thermographs of Ti6Al-MA-coarse after being held at 1200°C for various hold times

As the sintering time increases, the peak temperature is stabilizing around 1035°C and is becoming half the width and twice the height, as presented in Table 12 This is showing that the Aluminum diffusion is occurring and that the compact is becoming more chemically homogeneous.

Table 12 Exothermic peak characteristics of the sintering of Ti6Al-MA-coarse at different sintering time during the cooling phase

		Enthalpy (J/g)	Peak (°C)	Width 50% (°C)	Height (mW/mg)
Ti6Al-MA-coarse	**0 min**	58.58	892.7	260.6	0.1691
	15 min	64.32	1009.3	167.2	0.2650
	30 min	65.58	1045.9	138.5	0.3070
	45 min	64.36	1122.3	128.5	0.3230
	60 min	64.75	1034.8	122.0	0.3448
	Homo	58.8	1035	121	0.317

4.2.3 Calorimetry Analysis of Fully Homogenized Powder Compacts

Figure 36 is comparing the homogenized traces from each powder blend, from Figure 32, Figure 33, Figure 34 and Figure 35. As stated previously, the full homogenized curves presented on Figure 36 are the third cooling trace after sintering each powder blend for 120 minutes at 1200°C and then successively cooling them down to 20°C and heating them back to 1200°C three times (see Appendix D). The comparison of the homogenized powder blends highlights the differences of each powder addition in a fully sintered product.

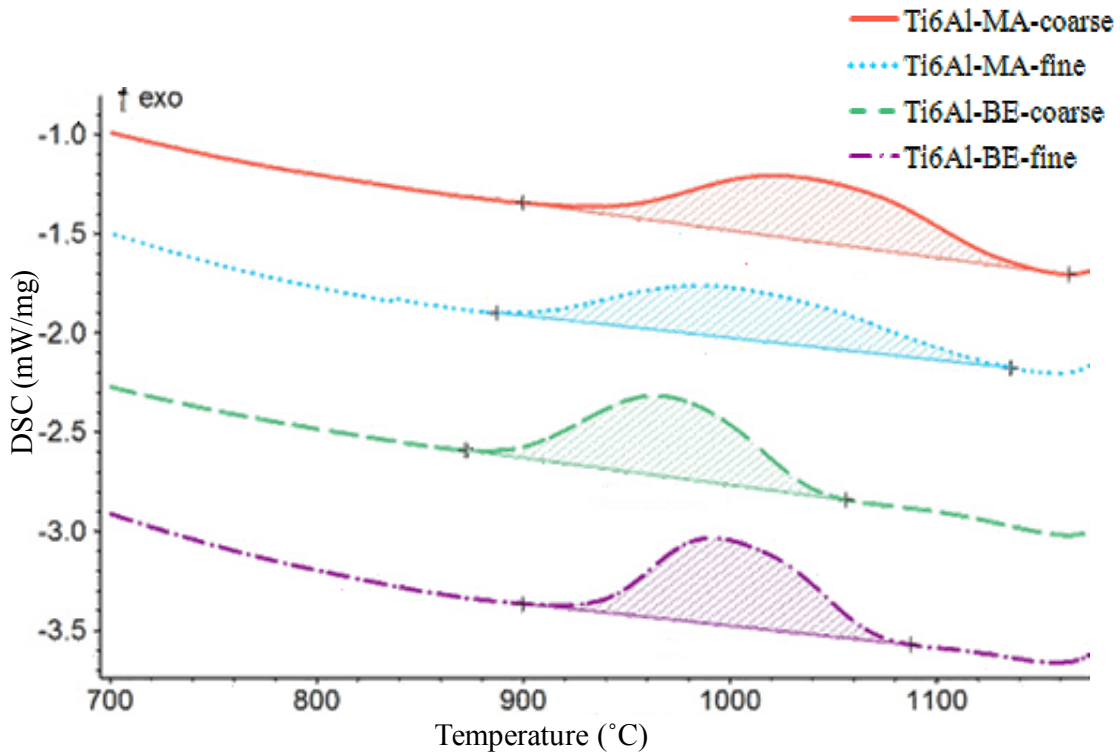

Figure 36 Cooling thermographs of the different powder blends fully homogenized

Powder blends with MA alloying additions are broader than the ones with BE additions. Fine powder additions' peaks are around 1000°C, where Ti6Al-BE-coarse is the lowest at 968°C and Ti6Al-MA-coarse the highest at 1035°C. However, the enthalpy of each powder source is very similar, averaging at 55.7 J/g with a standard deviation of 3.1 J/g, as presented in Table 13.

Table 13 Average values of the exothermic peak from the fully homogenized different powder blends

	Enthalpy (J/g)	**Peak (°C)**	**Width 50% (°C)**	**Height (mW/mg)**
Ti6Al-MA-coarse	58.8	1035	121	0.317
Ti6Al-MA-fine	51.5	1000	134	0.261
Ti6Al-BE-coarse	56.0	968	87	0.421
Ti6Al-BE-fine	56.5	994	84	0.444
Average	**55.7**	**999**	**107**	**0.36**
CP-Ti CP-Ti	***70.1***	***875***	***57***	***0.834***

As shown on the Titanium-Aluminum binary phase diagram, the temperature at which β phase starts transforming back to α phase is around 1000°C in Ti6Al, which is the peak temperature for Ti6Al-MA-fine and Ti6Al-BE-fine. Both have fine powder size additions, which reach chemical equilibrium faster. Ti6Al-BE-coarse's peak at 968°C is around the temperature where all the Ti6Al should be back to the α phase. Ti6Al-MA-coarse peak at 1035°C indicates that the β-to-α transformation starts at much higher temperature than the 1000°C that is expected for Ti6Al. It means that there are parts of the compacts where the concentration of Al is higher than 6wt%.

The peak broadness of compacts with MA additions indicates that, even though the compacts' peaks are not changing with each successive heating cycle, there is still a range of Titanium-Aluminum composition which is transforming back from β-to-α at a different temperature. Compacts with BE additions are 33% narrower than the ones with MA additions, which indicates that the composition range does not deviate a lot from Ti6Al.

Another explanation is that the percentage of impurities, Oxygen and Nitrogen, varies from one powder blend to the other. As discussed in section 1.3 and 4.2.2.3, O and N impurities affect the peak characteristics and the sintering response.

Figure 37 presents the aspect ratio of the peak width, measured at 50% of the peak height, over the peak height.

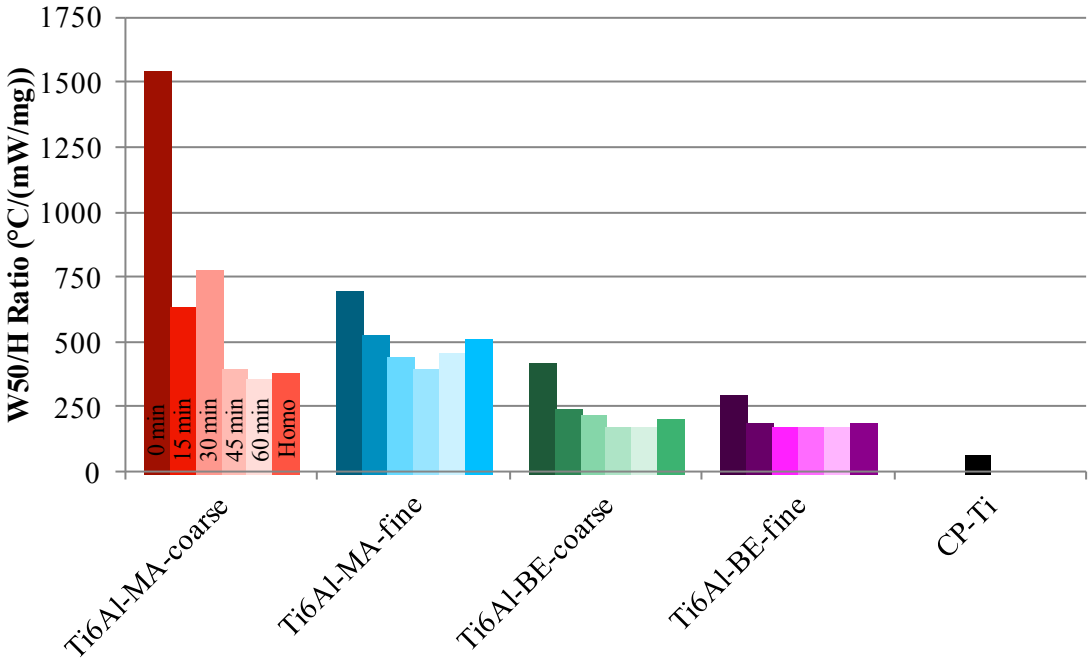

Figure 37 Aspect ratio of width over the height of the peak

Previous work [43] has shown that the aspect ratio of the width over the height is a good measure of homogeneity. The smaller the value of the ratio, the more homogenous the sample is.

In Figure 37, blends made from MA have a higher ratio than BE, Ti6Al-MA-coarse being the highest of all blends studied. As the sintering time increases, the ratio of all the compacts decreases. The most homogeneous, Ti6Al-BE-fine, is 2.75 times the ratio of CP-Ti while Ti6Al-MA-fine is 7.5 times higher than CP-Ti. Note that the MA mixtures W50/H ratio values may also be influenced by their higher O and N content.

BE blends become homogeneous between 15 and 30 minutes for Ti6Al-BE-fine and 30 and 45 minutes for Ti6Al-BE-coarse, as shown by the stability of the ratio after these sintering times have elapsed.

4.2.4 Microscopy Analysis of Sintered Compacts

Figure 38 presents the microstructure of Ti6Al-MA-coarse after being sintered for 0min, 30min, and 60min. After no hold time, as presented on Figure 38 (a), the microstructure is quite inhomogeneous with a large area that appears dark in reaction with the etchant (low or no Aluminum content) and brighter spots which surround the former MA-coarse particle. The 0 min situation appears to be barely more homogenous than the sample heated up at 1050°C on Figure 28 (c). This also confirms the DSC observation on Figure 35, where the trace with no hold time is quite wide with two peaks. As the sintering time increases, the compact becomes more homogeneous, as shown on Figure 38 (b) and (c). This also ties back to the DSC observation of Figure 35 where the peak narrows as the compact gets more homogeneous.

The comparison of different powder source can be done by taking a look at Figure 39, which presents the microstructure of Ti6Al-BE-coarse after being sintered for 0min, 30min, and 60min. The microstructure has evolved from being inhomogeneous scattered powder particles of Titanium surrounded by an Aluminum-rich outer layer at 1050°C on Figure 27 (c), to a more homogeneous microstructure on Figure 39. There is no notable difference on the microstructure between the sintering time, and the aspect ratio of the DSC peak do not noticeably change either.

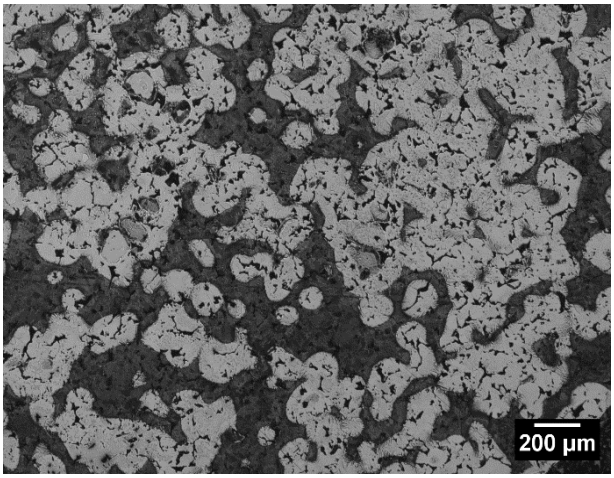

(a)

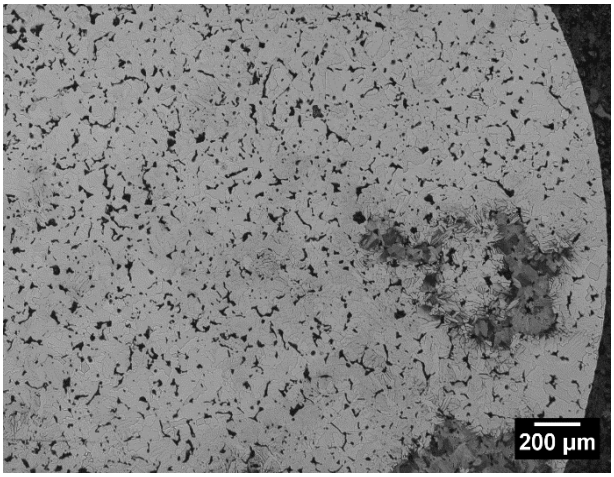

(b)

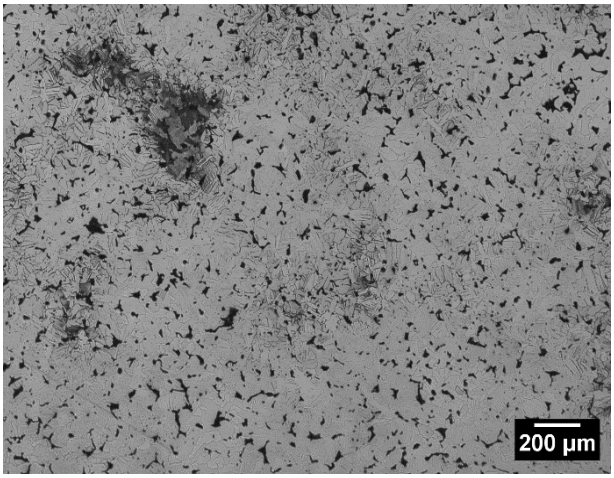

(c)

Figure 38 Microstructure of Ti6Al-MA-coarse sintered for (a) 0 min, (b) 30 min and (c) 60 min

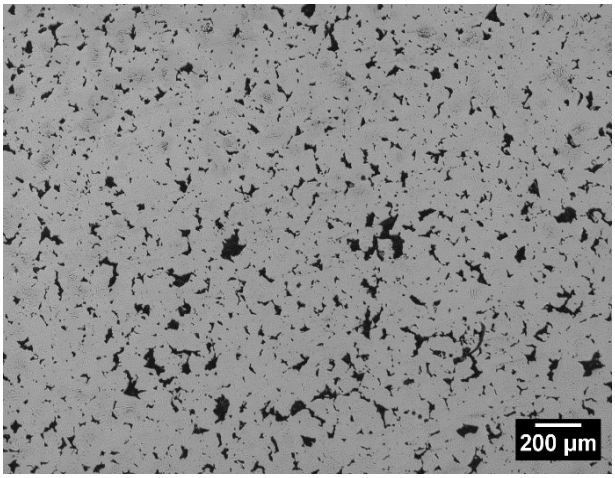

(a)

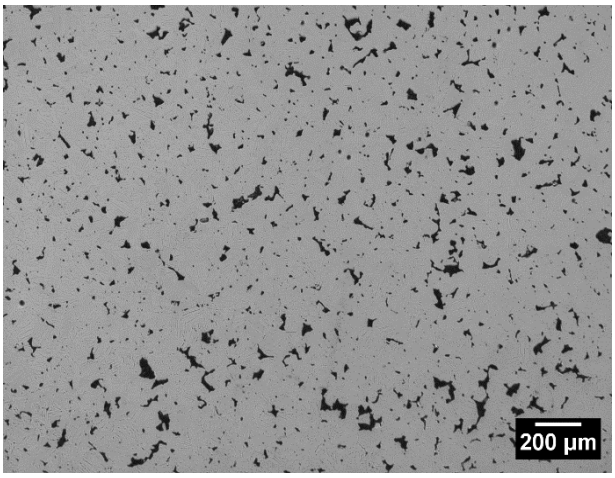

(b)

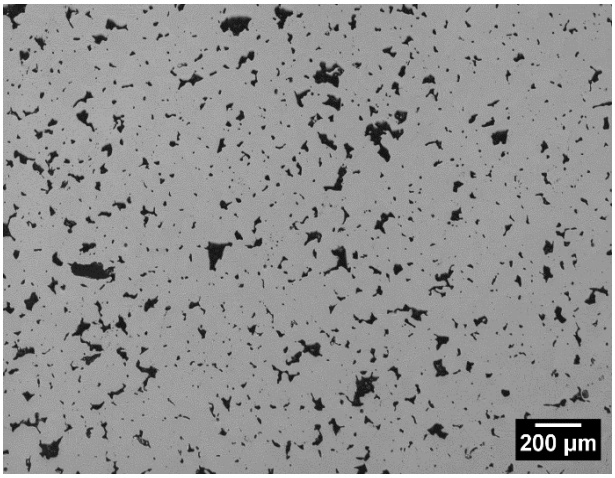

(c)

Figure 39 Microstructure of Ti6Al-BE-coarse sintered for (a) 0 min, (b) 30 min and (c) 60 min.

4.2.5 Microscopy Analysis of Fully Homogenized Compacts

Figure 40 shows that the sintered compacts are chemically homogeneous with the Aluminum fully diffused into the CP-Ti matrix, unlike that shown in Figure 38. It also shows that the pore patterns are quite different for each powder blend.

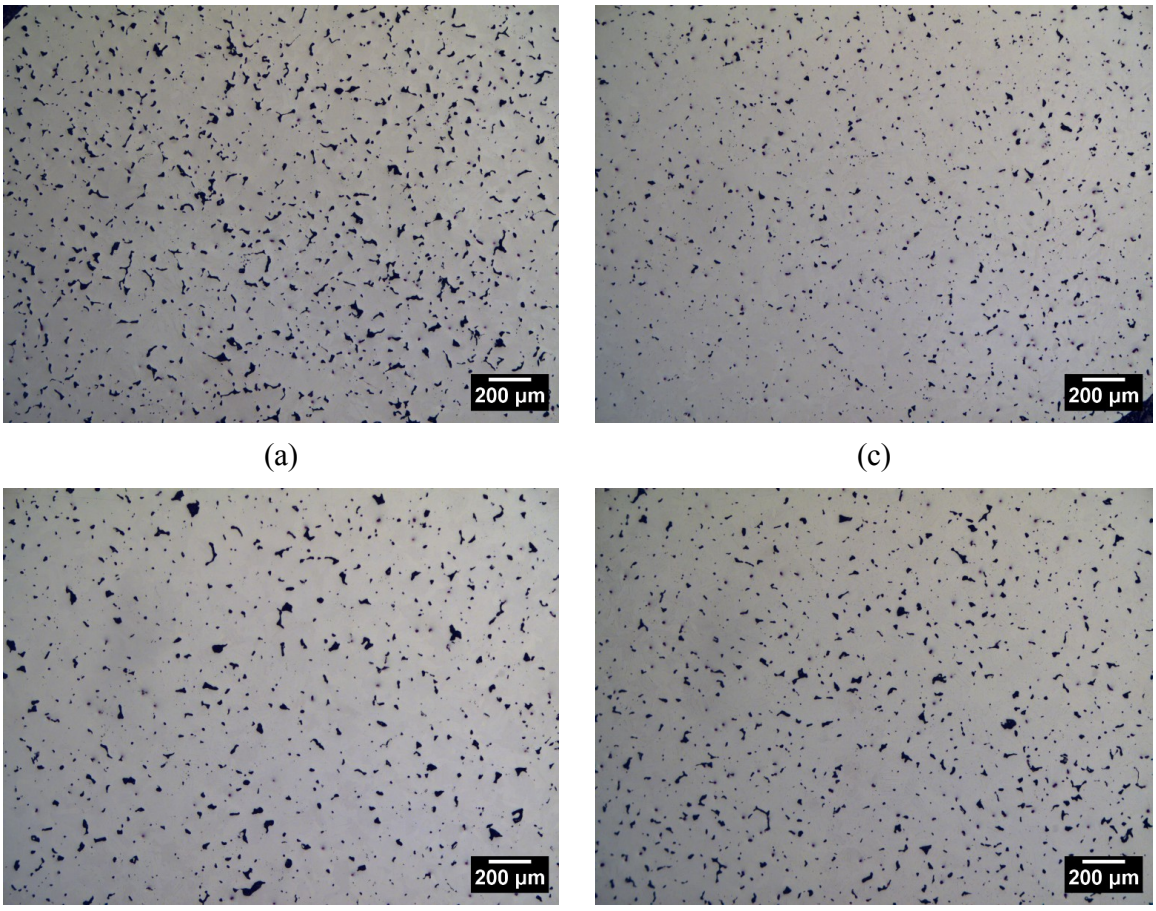

(a) (c)

(b) (d)

Figure 40 Pore systems of homogenized powder blend: (a) Ti6Al-MA-coarse, (b) Ti6Al-BE-coarse, (c) Ti6Al-MA-fine and (d) Ti6Al-BE-fine

Fine powder blends are generating smaller pores for both the master alloy and the blended elemental addition. However, Ti6Al-MA-fine shows more densification than all compacts. Its pores are the smallest and there are less of them than in any other powder blend. The difference between fine and coarse blended elemental addition is much smaller than between the fine and coarse master alloy. Section 4.3 will use dilatometry and compact measurements to investigate the densification behaviour further.

4.3 Densification

4.3.1 Densification Study using Dilatometry

Figure 41 presents the dilatometry traces of the different powder compacts during a sintering cycle with a one hour hold time at 1200°C. BE compacts were heated up at 10°C/min until 100°C and then at 20°C/min up to 1200°C. MA compacts were heated up to 150°C at 8°C/min and then at 20°C/min to 1200°C. All compacts were heated up at the same heating rate of 20°C/min and were held for one hour at 1200°C. Figure 42 provides more detail on the heating stage only.

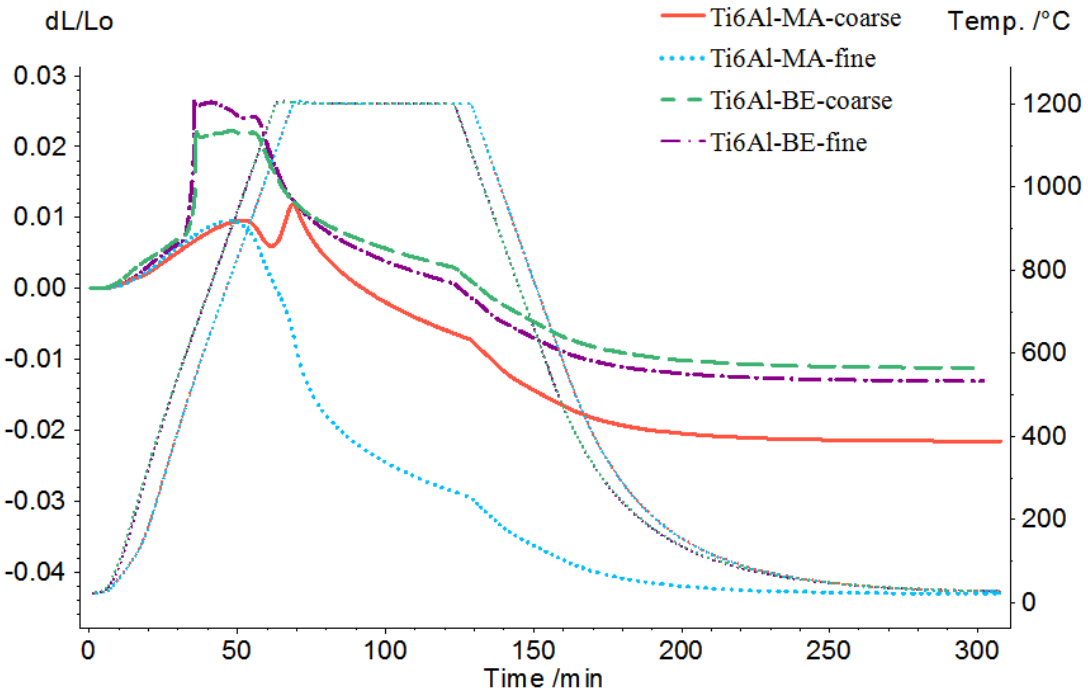

Figure 41 Dilatometry traces showing the different blend powders while sintering

All compacts are slowly expanding during heating due to the thermal expansion in the samples. BE compacts display a rapid expansion, starting at a little over 600°C that turns into a plateau up to 1070°C. There is no such rapid expansion displayed in the MA compacts, which appear to start densifying a little above 900°C. However, Ti6Al-MA-coarse begins to expand from 1050°C to 1200°C, as shown on Figure 42, before shrinking again during the hold at 1200°C.

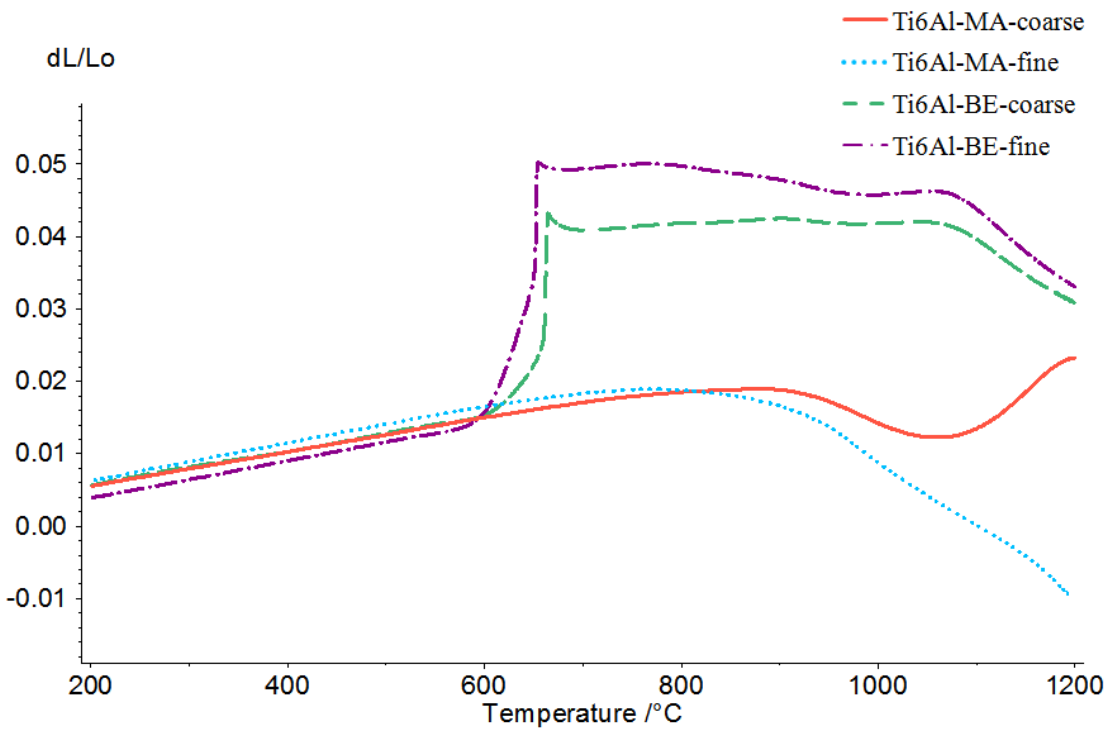

Figure 42 DIL traces of the different powder blends during heating to 1200°C at 20°C/min

Table 14 presents the variation in length, as measured by the dilatometer, for each powder blend after being sintered for 1h in vacuum conditions.

Table 14 Variation in length from the dilatometer for each powder blend

	dL/Lo ($*10^{-3}$)	**%**
Ti6Al-MA-coarse	- 21.5127	-2.2%
Ti6Al-MA-fine	- 41.5528	-4.2%
Ti6Al-BE-coarse	- 13.7557	-1.4%
Ti6Al-BE-fine	- 14.06445	-1.4%

The expansion of the blended elemental samples around 660°C is due to the exothermic reaction generated by pure liquid Aluminum forming intermetallics that left large pores behind. Another interesting feature of Figure 41 is the dip seen in Ti6Al-MA-coarse trace at around 1050°C. The compact starts to shrink but then expands rapidly up to the maximum temperature of 1200°C before densifying again with the sintering process. This unique behaviour in the coarse MA mixture is expected to be due to the lower level of interdiffusion and homogenization that has occurred in this sample as evidenced by the

1050 °C micrograph of Figure 29 (a). There is a high volume fraction of the original TiAl MA particles still present in the structure. A diffusion couple forms around these particles such that the bright white boundary visible at the pure Ti/TiAl interface is Ti_3Al. From the binary phase diagram of Figure 9, it can be seen that at 1120 °C the α-Ti phase would form at the Ti_3Al/TiAl interface through the eutectoid reaction, Ti_3Al + TiAl = α-Ti. It is expected that this complex phase transformation leads to the unique dilatational behaviour in the coarse MA blend.

4.3.2 Densification Analysis using Compact Measurements

Table 15 takes a look at the compact measurement difference. A caliper vernier is not as sensitive as the dilatometer to detect length variations, but it can confirm is the trend is followed.

Table 15 Comparison between dilatometer measured difference in length and compact measurements

	DIL		Compact		Deviation
	dL/Lo (*10^{-3})	**%**	**dL/Lo (*10^{-3})**	**%**	**%**
Ti6Al-MA-coarse	- 21.51	-2.2%	- 17.16	-1.7%	0.4%
Ti6Al-MA-fine	- 41.55	-4.2%	- 40.54	-4.1%	0.1%
Ti6Al-BE-coarse	- 13.76	-1.4%	- 8.49	-0.8%	0.5%
Ti6Al-BE-fine	- 14.06	-1.4%	- 9.44	-0.9%	0.5%

DIL compacts are longer than DSC compacts which make them easier to measure, thus the deviation measured is more reliable. Since the DIL only records the variation in the longitudinal direction, there is no certain way to assess what the radial variation is. The calculation of density from the physical dimensions of the compact presented in Table 16 sheds some light on the effect of sintering on the density of the compact.

Table 16 Effect of sintering on density using compacts measurements according to alloying element and powder size

	Green density (g/cc)	**Sintered density (g/cc)**	**% increase in density**
Ti6Al-MA-coarse	3.43	3.61	5.10%
Ti6Al-MA-fine	3.52	3.98	13.26%
Ti6Al-BE-coarse	3.71	3.85	3.80%
Ti6Al-BE-fine	3.77	3.92	4.07%

The densities calculated from the physical measurements of the compacts concur with the DIL measurements. The density of Ti6Al-MA-fine increased the most. It is interesting to note that the sintered density of Ti6Al-MA-fine and Ti6Al-BE-fine is similar, 3.98 g/cc and 3.92 g/cc, but their green densities were considerably different. BE blends appear to be easier to compact, with pure Al being more ductile that TiAl MA. More focus would need to be placed on the compaction of green samples made from MA powders to benefit fully from its superior densification.

Chapter 5. Conclusions and Future Work

The advantage of powder metallurgy is its lower cost. In the case of Titanium PM, a further potential cost benefit is the use of a lower cost Titanium powder source. In this investigation, a coarse HDH CP-Ti powder source was chosen as it represented the lowest cost commercially available powder. The challenge is to use this coarse powder in a sintering operation to create alloys of a specific composition that are homogeneous and dense.

Aluminum is the main alloying addition in most commercial Titanium alloys. Therefore this study focussed on the sintering behaviour of a base Ti-6Al alloy as a function of different Al containing powder additions. The results of the study show that the powder size and the powder form, i.e. BE or MA, of the Aluminum addition affects sintering behaviour. Table 17 summarizes the effect of each powder addition on the sintering behaviour of Titanium-Aluminum alloys.

Table 17 Summary of the alloying additions effect on densification and diffusion

	Fine		**Coarse**	
Blended Elemental	Poor densification	Fast homogenization	Poor densification	Medium homogenization
Master Alloy	High densification	Fair homogenization	Medium densification	Poor homogenization

The different techniques used demonstrated that sintering behaviour varied depending on the powder source. The study of the DSC exothermic cooling peak width highlighted the homogenization sintering time, which is the fastest in Ti6Al-BE-fine with stable homogenization after sintering for around 15 min at 1200°C and the slowest with Ti6Al-MA-coarse. This is confirmed by the microscopy observations. Densification was observed by the use of DIL and optical microscopy. MA powder additions, especially Ti6Al-MA-fine, displayed higher densification than BE powder blends due to the exothermic reaction generated by pure Al that left large pores behind.

DSC is a powerful tool to investigate the reaction and phase transformation and was used successfully to investigate the sintering behaviour and the alloying of compacts with different powder source.

5.1 Future Work

The evaluation of chemical homogeneity and density during sintering gives an indication about the likely mechanical response of the sintered compacts. As a consequence, the next logical step is to assess the mechanical properties (Young's Modulus, Elastic Strength and Ultimate Strength) of the chosen powder blend. These mechanical properties can be reliably obtained by using a tensile test or, alternatively, a three-point bending test.

It would be interesting to find if the fully homogenized compacts display ductile behavior, although it is also important to note these properties will be affected by oxygen content. In addition, it would be interesting to validate if the model of Lu et al. [52] for the Young's modulus of low porosity materials, $E = E_0(1 - 2\Phi)(1 + 4\Phi^2)$, to see if this successfully represents the Young's Modulus for the Ti6Al sintered blends.

SEM and XRD could be used to further the understanding of the intermetallics that are generated during the heating stage (i.e. for samples cooled down at 100°C/min) and the isothermal hold sections.

Finally, combining this research with the prior work conducted on Ti-2.5Fe [43] could lead to a better understanding of the influence of different additions in the powder metallurgical development of the Ti-5Al-2.5Fe ternary system, and help the development of a viable manufacturing route for Titanium alloys in the automotive industry.

Bibliography

[1] G. Lütjering and J. C. Williams, *Titanium*, 2nd ed. Berlin ; New York: Springer, 2007.

[2] J. F. Cannon, "Behavior of Elements at High Pressures," *J. Phys.. Chem. Ref. Data*, vol. 3, no. 3, pp. 781–817, 1974.

[3] Y. Yamashita, I. Takayama, H. Fujii, and T. Yamazaka, "Nippon Steel Technical Report #85," 2002.

[4] M. J. Donachie, "A Primer on Titanium and Its Alloys," in *Titanium - A Technical Guide*, 2nd ed., ASM International, 2000, pp. 1–3.

[5] M. Ashby, H. Shercliff, and D. Cebon, *Materials: Engineering, Science, Processing and Design*, 2nd ed. Elsevier, 2010.

[6] W. F. Smith, "Titanium and its alloys," in *Structure and properties of engineering alloys*, 2nd ed., McGraw-Hill, 1993, p. 630.

[7] Special Metals Corporation, "INCONEL alloy 625," 2006.

[8] "Metals," *MetalPrices.com*, 2013. [Online]. Available: http://www.metalprices.com/. [Accessed: 09-Aug-2013].

[9] R. Boyer, "An overview on the use of titanium in the aerospace industry," *Mater. Sci. Eng. A*, vol. 213, no. 1–2, pp. 103–114, Aug. 1996.

[10] K. Faller and F. H. S. Froes, "The use of titanium in family automobiles: Current trends," *JOM*, vol. 53, no. 4, pp. 27–28, Apr. 2001.

[11] MatWeb LLC, "Material property data," 2013. [Online]. Available: http://www.matweb.com/index.aspx. [Accessed: 14-Aug-2013].

[12] A. Zhecheva, W. Sha, S. Malinov, and A. Long, "Enhancing the microstructure and properties of titanium alloys through nitriding and other surface engineering methods," *Surf. Coatings Technol.*, vol. 200, no. 7, pp. 2192–2207, 2005.

[13] R. Perry, "The thermodynamics of phase transitions," *Computer Simulation of Alloys meeting*. Edinburgh, 2010.

[14] T. Nishimura, T. Mizoguchi, and Y. Itoh, "Titanium materials for cryogenic services," *R D Res. Dev. Kobe Steel Eng. Reports*, vol. 34, no. 3, p. 63, 1984.

[15] EHKTechnologies, "Summary of Emerging Titanium Cost Reduction Technologies," Vancouver, WA, 2004.

[16] S. J. Gerdemann, "TITANIUM Process Technologies.," *Adv. Mater. Process.*, vol. 159, no. 7, p. 41, Jul. 2001.

[17] G. Chen, D. Fray, and T. Farthing, "Direct electrochemical reduction of titanium dioxide to titanium in molten calcium chloride," *Nature*, vol. 407, no. 6802, pp. 361–4, Sep. 2000.

[18] M. J. Donachie, "Powder Metallurgy," in *Titanium - A Technical Guide*, 2nd ed., no. c, ASM International, 2000, pp. 47–53.

[19] C. G. McCraken, “Production of fine titanium powders via the Hydride- Dehydride (HDH) process,” *Powder Inject. Mould. Int.*, vol. 2, no. 2, 2008.

[20] O. D. Neikov, S. S. Naboychenko, I. V. Murashova, V. G. Gopienko, I. V. Frishberg, and D. V. Lotsko, “Atomization and Granulation,” in *Handbook of Non-Ferrous Metal Powders*, Elsevier Ltd., 2008.

[21] J. Schuster and M. Palm, “Reassessment of the binary Aluminum-Titanium phase diagram,” *J. Phase Equilibria Diffus.*, vol. 27, no. 3, pp. 255–277, 2006.

[22] “Titanium-Aluminum (Ti-Al) Phase Diagram,” 2008. [Online]. Available: http://www.calphad.com/. [Accessed: 14-Aug-2013].

[23] *ASM Handbook Volume 03: Alloy Phase Diagrams*. ASM International, 1992.

[24] M. Sujata, S. Bhargava, and S. Sangal, “On the formation of TiAl3 during reaction between solid Ti and liquid Al,” *J. Mater. Sci. Lett.*, vol. 16, no. 13, pp. 1175–1178, 1997.

[25] U. R. Kattner, J.-C. Lin, and Y. A. Chang, “Thermodynamic Assessment and Calculation of the Ti-Al System,” *Metall. Trans. A*, vol. 23, no. 8, pp. 2081–2090, 1992.

[26] H. Okamoto, “O-Ti (Oxygen-Titanium),” vol. 32, no. 5, pp. 473–474, 2011.

[27] H. Okamoto, “N-Ti (Nitrogen-Titanium),” *J. Phase Equilibria Diffus.*, vol. 34, no. 2, pp. 1–2, 2012.

[28] S.-J. L. Kang, “Sintering densification, grain growth, and microstructure.” Elsevier Butterworth-Heinemann, Amsterdam; Boston; London, 2005.

[29] R. M. German, *Powder metallurgy and particulate materials processing : the processes, materials, products, properties and applications*. Princeton, New Jersey: Metal Powder Industries Federation, 2005.

[30] R. M. German, *Powder metallurgy science*, 2nd ed. Princeton, N.J.: Metal Powder Industries Federation, 1994.

[31] Materials Solutions, “Thermal Analysis Tests,” *BIS - The Department for Business Innovation and Skills (UK)*, 2004. [Online]. Available: http://www.materialssolutions.info.

[32] W. F. Günther Höhne and H.-J. F. Hemminger, *Differential Scanning Calorimetry*, 2nd ed. Springer-Verlag Berlin Heidelberg New York, 2003.

[33] A. Schindler and B. Jürgen, “The Benchmark in High-Temperature DSC: The New DSC 404 Pegasus,” *OnSet*, pp. 14–26, 2008.

[34] E. J. Mittemeijer, *Fundamentals of materials science: The microstructure-property relationship using metals as model systems*. 2011.

[35] Automotive Partnership Canada, “Research aims to make titanium an affordable alternative to steel,” 2012. [Online]. Available: www.apc-pac.ca. [Accessed: 27-Sep-2013].

[36] C. G. McCraken, C. Motchenbacher, and D. P. Barbis, “Review of Ti powder

production methods McCracken, Motchenbacher & Barbis Int J of Powder Met 2010.pdf," *Int. J. Powder Metall.*, vol. 46, no. 5, pp. 19–26, 2010.

[37] I. M. Robertson and G. B. Schaffer, "Review of densification of titanium based powder systems in press and sinter processing," *Powder Metall.*, vol. 53, no. 2, pp. 146–162, May 2010.

[38] L. Bolzoni, P. G. Esteban, E. M. Ruiz-Navas, and E. Gordo, "Mechanical behaviour of pressed and sintered titanium alloys obtained from prealloyed and blended elemental powders.," *J. Mech. Behav. Biomed. Mater.*, vol. 14, pp. 29–38, Oct. 2012.

[39] G. Steedman and S. F. Corbin, "Determining sintering mechanisms and rate of *in situ* homogenisation during master alloy sintering of Ti6Al4V," *Powder Metall.*, vol. 58, no. 1, pp. 67–80, 2015.

[40] W. Chen, Y. Yamamoto, W. H. Peter, M. B. Clark, S. D. Nunn, J. O. Kiggans, T. R. Muth, C. A. Blue, J. C. Williams, and K. Akhtar, "The investigation of die-pressing and sintering behavior of ITP CP-Ti and Ti-6Al-4V powders," *J. Alloys Compd.*, vol. 541, pp. 440–447, Nov. 2012.

[41] O. M. Ivasishin, V. M. Anokhin, A. N. Demidik, and D. G. Savvakin, "Cost effective blended elemental powder metallurgy of Ti alloys for transportation application," *Key Eng. Mater.*, vol. 188, pp. 55–62, 2000.

[42] R. P. Siqueira, H. R. Z. Sandim, A. O. F. Hayama, and V. A. R. Henriques, "Microstructural evolution during sintering of the blended elemental Ti–5Al–2.5Fe alloy," *J. Alloys Compd.*, vol. 476, no. 1–2, pp. 130–137, May 2009.

[43] J. O'Flynn and S. F. Corbin, "The influence of iron powder size on pore formation, densification and homogenization during blended elemental sintering of Ti–2.5Fe," *J. Alloys Compd.*, vol. 618, pp. 437–448, 2015.

[44] B. B. Panigrahi, N. S. Reddy, K. Sad, and M. M. Godkhindi, "Dilatometric sinytering of Ti-2Al and Ti-5Al elemental powders," *J. Mater. Sci. Technol.*, vol. 23, no. 3, pp. 363–366, 2007.

[45] A. Cezairliyan and A. P. Miiller, "Thermodynamic study of the alpha beta phase transformation in titanium by a pulse heating method," *J. Res. Natl. Bur. Stand. (1934).*, vol. 83, no. 2, p. 127, Mar. 1978.

[46] Y. Su, D. Zhang, F. Kong, and Y. Chen, "Microstructure and mechanical properties of TiAl alloys produced by rapid heating and open die forging of blended elemental powder compacts," *Mater. Sci. Eng. A*, vol. 563, no. 0, pp. 46–52, 2013.

[47] ASTM International, "B214 -07 Standard Test Method for Sieve Analysis of Metal Powders," no. Reapproved 2011, pp. 1–5, 2014.

[48] "NETZSCH Proteus Software for Thermal Analysis." [Online]. Available: https://www.netzsch-thermal-analysis.com/en/products-solutions/software/proteus/. [Accessed: 24-May-2016].

[49] J. Schindelin, C. T. Rueden, M. C. Hiner, and K. W. Eliceiri, "The ImageJ

ecosystem: An open platform for biomedical image analysis," *Mol. Reprod. Dev.*, vol. 82, no. 7–8, pp. 518–529, Jul. 2015.

[50] P. Bishop and P. Scallion, "Hitachi S-4700 Field Emission Scanning Electron Microscope," 2013. [Online]. Available: http://www.dal.ca/dept/irm/fmc.html. [Accessed: 24-May-2016].

[51] S. Malinov, Z. Guo, W. Sha, and A. Wilson, "Differential Scanning Calorimetry Study and Computer Modeling of beta->alpha Phase Transformation in a Ti-6Al-4V Alloy," vol. 32, no. April, 2001.

[52] G. Lu, G. Q. (Max) Lu, and Z. M. Xiao, "Mechanical Properties of Porous Materials," *J. Porous Mater.*, vol. 6, no. 4, pp. 359–368, 1999.

Appendix A: Particle Size Distribution

About 25% of TiAl is under 25µm and has been selected as TiAl-fine prealloyed addition. Similarly, about 25% of the TiAl powder is above 45µm which constitutes the TiAl-coarse prealloyed addition. The full spectrum of the coarse Aluminum powder, with a D_{50} of 43.1µm, is used in the Ti6Al-BE-coarse mixture. Fine Aluminum powder has a narrow size band and a D_{50} of 12.7µm. CP-Ti has a D_{50} of 109.9 µm which is typical of Titanium powders made with the HDH technique, as presented in Table 3.

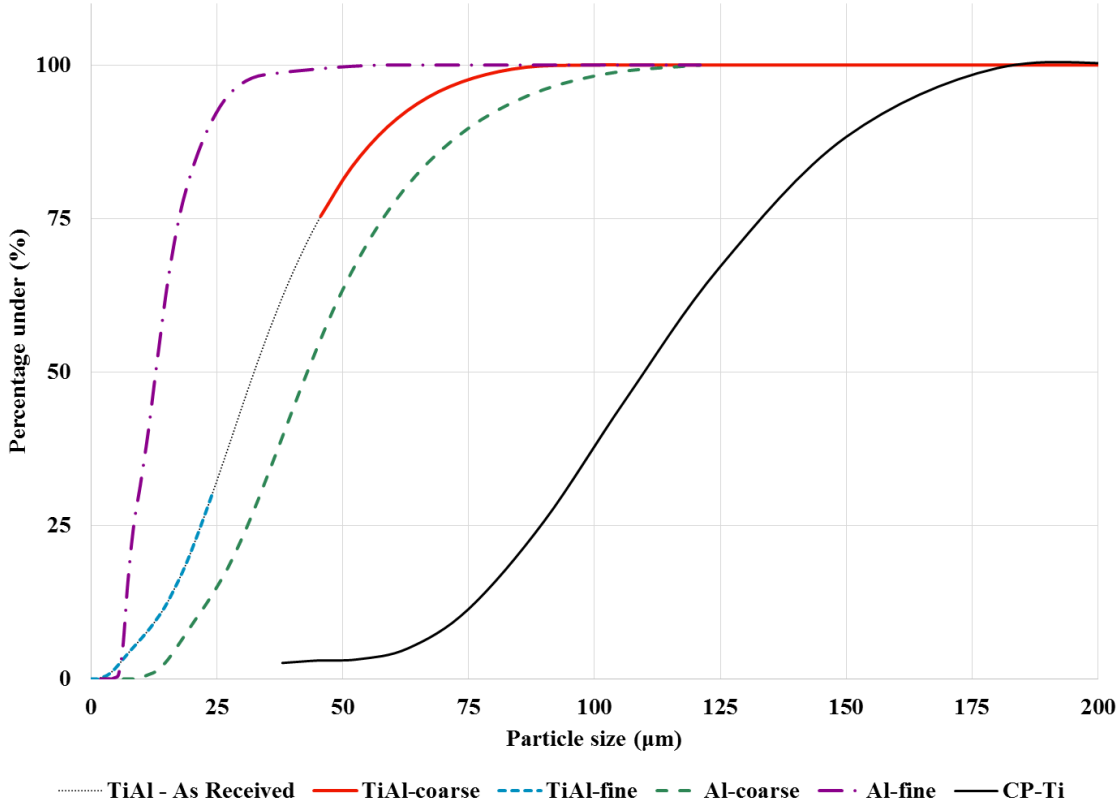

Figure 43 Particle size distribution of the alloying additions

Appendix B: Determination of the Chemical Composition of TiAl-coarse

Analysis from ATI provided the chemical composition of the powder TiAl with the coarse powder removed (TiAl, mesh <325). Since the bulk chemical composition and the composition below mesh 325 are known, it is possible to calculate:

$$Chemical\ composition\ of\ TiAl\text{-}coarse = \frac{(A - B * b)}{c} \qquad (V)$$

where

A = Bulk chemical composition of TiAl

B = Chemical composition of TiAl without TiAl-coarse

b = Fraction of TiAl without TiAl-coarse

c = Fraction of TiAl-coarse in bulk TiAl

Examples of calculation for chemical content in TiAl-coarse

C: (0.079% - 0.075% * 0.95)/0.05 = 0.155%

H: (0.014% - 0.013% * 0.95)/0.05 = 0.033%

O: (0.69% - 0.70% * 0.95)/0.05 = 0.50%

N: (0.300% - 0.260% * 0.95)/0.05 = 1.06%

Appendix C: Determination of the Chemical Composition of the Blends

The composition of the powder blends can be obtained, for each chemical component studied, using the following formula:

$$Blend\ Composition = Composition\ M * weight\ \%\ M + Composition\ A * weight\ \%\ A \quad \text{(IV)}$$

where

M = matrix (CP-Titanium)

A = powder addition (TiAl-coarse, TiAl-fine, Al-coarse or Al-fine)

Examples of calculation for O_2 content in powder blends

Ti6Al-MA-coarse: 0.179%*0.64+0.5%*0.36 = 0.2946 wt%

Ti6Al-MA-fine: 0.179%*0.64+0.94%*0.36 = 0.4530 wt%

Ti6Al-BE-coarse: 0.179%*0.94+0.132%*0.06 = 0.1762wt%

Ti6Al-BE-fine: 0.179%*0.94+0.54%*0.06 = 0.2007wt%

Appendix D: Homogenization at 1200°C

Compacts were heated up to 1200°C and held at this temperature for 2 hours. They were then cooled down to room temperature at 40°C/min and successively heated back up to 1200°C and cooled down, with no hold time. Table 18 presents the exothermic peak values for three successive cooling cycles and their variation. The peak temperature variation is 3°C or less for all compacts, and the coefficient of variation of the area (a combination of width and height values) is 2.5% or less, which indicates that the compacts have reached a stable state.

Table 18 Data from the exothermic peak of successive heating and cooling cycles to assess the homogeneity of the compact at 1200°C

		Enthalpy (J/g)	**Peak (°C)**	**Width (°C)**	**Height (mW/mg)**
Ti6Al-MA-coarse	1	58.09	1034.1	118.1	0.3169
	2	59.45	1035.8	122.8	0.3193
	3	58.92	1036.4	123.1	0.3143
	Average	58.8	1035	121	0.317
	STDEV	0.7	1.2	2.8	0.0
	Variation	**1.17%**	**0.12%**	**2.31%**	**0.79%**
TiAl-MA-fine	1	52.92	995.0	130.9	0.2678
	2	52.81	1000.0	135.0	0.2603
	3	51.47	999.8	135.5	0.254
	Average	52.4	998	134	0.261
	STDEV	0.8	2.8	2.5	0.0
	Variation	**1.54%**	**0.28%**	**1.89%**	**2.65%**
Ti6Al-BE-coarse	1	56.99	966.5	85.2	0.4376
	2	56.46	968.4	87.2	0.4230
	3	54.47	969.4	89.1	0.4031
	Average	56.0	968	87	0.421
	STDEV	1.3	1.5	2.0	0.0
	Variation	**2.37%**	**0.15%**	**2.24%**	**4.11%**
Ti6Al-BE-fine	1	57.01	993.6	83.1	0.4562
	2	56.24	995.1	84.1	0.4427
	3	56.11	993.4	85.0	0.4336
	Average	56.5	994	84	0.444
	STDEV	0.5	0.9	1.0	0.0
	Variation	**0.86%**	**0.09%**	**1.13%**	**2.56%**

Reference 1: Chemical Analysis (TiAl As Received)

ATI Wah Chang

Analytical Services
1600 Old Salem Rd NE
Albany, Or. 97321

Office: 541-967-6918
1-888-926-4211 ext 6918
Fax: 541-967-6986
www.wahchanglabs.com

Report Of Analysis

Report Id: 100577077_V1 Total pages: 1

September 27, 2013

DALHOUSIE UNIVERSITY
1360 Barrington St
Building F
Room 201
Halifax Nova Scotia, B3J 1Z1
CANADA

Attention : Julian O'Flynn

MATERIAL IDENTITY --- TI AL
PURCHASE ORDER --- CC
TURNAROUND TIME --- Normal

pct ----- percent
ppm ..... parts per million (by weight)

WC Sample ID	Client ID
J-231386 ---	TI AL

WC Sample ID: J - 231386

C	ppm	790
LECO CS-444	ORIGINAL	
H	ppm	140
LECO RH-404 UNIT 2	ORIGINAL	
N	ppm	3000
LECO TC-436 UNIT 2	ORIGINAL	
O	pct	0.69
LECO TC-436 UNIT 2	ORIGINAL	

BILL BEASLEY /es
Analytical Laboratory Expeditor

Accredited Nadcap

The measurement uncertainty associated with the data on this report of analysis is available from the laboratory upon request.

The "/es" signifies this document has been electronically signed by the person named.

The ISO/IEC 17025:2005 scope of accreditation is limited to material analyzed by the following instruments: LECO CS-444, LECO CS-600, LECO TC-436, LECO TC-600, LECO RH-404, DCP6, DCP7, SPECTRO ICP-OES.09, SPECTRO ICP.10, SPECTRO ICP-OES.11, SPECTRO ICP-OES.12, VG PLASMAQUAD+, PE MS ELAN 9000 and THERMO SCIENTIFIC X SERIES. Certificate available upon request.

The Nadcap scope of accreditation is limited to titanium-based material analyzed by the following instruments: LECO CS-444, LECO CS-600, LECO TC-436, LECO TC-600, LECO RH-404, DCP7, SPECTRO ICP-OES.09, SPECTRO ICP.10, SPECTRO ICP-OES.11, SPECTRO ICP-OES.12, VG PLASMAQUAD+, PE MS ELAN 9000 and THERMO SCIENTIFIC X SERIES. Certificate available upon request.

Analysis Disclaimer: This "Report of Analysis" is intended only to document the analytical results obtained. There has been no review of specification requirements for the material tested and therefore the test results do not certify that the submitted sample results meet any specification.

The analysis results were produced in accordance with ATI Wah Chang work instruction WI-AL-35 (current version), where applicable. Rounding is per ASTM E-29.

Reference 2: Chemical Analysis of TiAl-fine and TiAl (mesh <325)

ATI Specialty Alloys & Components

Analytical Services
1600 Old Salem Rd NE
Albany, Or. 97321

Office: 541-967-6913
1-888-926-4211 ext 6913
Fax: 541-967-6986

Report Of Analysis

Report Id: 100613563_V1 Total pages: 1

March 25, 2015

DALHOUSIE UNIVERSITY
1360 Barrington St
Building F
Room 201
Halifax Nova Scotia, B3J 1Z1
CANADA

Attention : Julian O'Flynn

MATERIAL IDENTITY --- TI-AL POWDER
PURCHASE ORDER --- CC
TURNAROUND TIME --- Normal

WC Sample ID	Client ID
J-246699 ---	TIAL-SIEVED-325
J-246700 ---	TIAL-FINE-500

pct ..... percent
ppm ..... parts per million (by weight)

WC Sample ID:	J -	246699	246700
C LECO CS-444	ppm ORIGINAL	750	960
H LECO RH-404	ppm ORIGINAL	130	170
N LECO TC-436	ppm ORIGINAL	2600	3500
O LECO TC-436	pct ORIGINAL	0.70	0.94

LISA HOLIFIELD /es
Analytical Laboratory Expeditor

Accredited Nadcap

The measurement uncertainty associated with the data on this report of analysis is available from the laboratory upon request.

The "/es" signifies this document has been electronically signed by the person named.

The ISO/IEC 17025:2005 scope of accreditation is limited to material analyzed by the following instruments: LECO CS-444, LECO CS-600, LECO TC-436, LECO TC-600, LECO RH-404, DCP6, DCP7, SPECTRO ICP-OES.09, SPECTRO ICP.10, SPECTRO ICP-OES.11, SPECTRO ICP-OES.12, VG PLASMAQUAD+, PE MS ELAN 9000 and THERMO SCIENTIFIC X SERIES. Certificate available upon request.

The Nadcap scope of accreditation is limited to titanium-based material analyzed by the following instruments: LECO CS-444, LECO CS-600, LECO TC-436, LECO TC-600, LECO RH-404, DCP7, SPECTRO ICP-OES.09, SPECTRO ICP.10, SPECTRO ICP-OES.11, SPECTRO ICP-OES.12, VG PLASMAQUAD+, PE MS ELAN 9000 and THERMO SCIENTIFIC X SERIES. Certificate available upon request.

Analysis Disclaimer: This "Report of Analysis" is intended only to document the analytical results obtained. There has been no review of specification requirements for the material tested and therefore the test results do not certify that the submitted sample results meet any specification.

The analysis results were produced in accordance with ATI Specialty Alloys and Components work instruction WI-AL-35 (current version), where applicable. Rounding is per ASTM E-29.